Monthly Notices
of the
ROYAL ASTRONOMICAL SOCIETY

MNRAS **505,** 1661–1677 (2021)
Advance Access publication 2021 May 12

https://doi.org/10.1093/mnras/stab1287

AT2017gfo: Bayesian inference and model selection of multicomponent kilonovae and constraints on the neutron star equation of state

Matteo Breschi [1]★ Albino Perego,[2,3] Sebastiano Bernuzzi [1] Walter Del Pozzo [4,5] Vsevolod Nedora [1] David Radice[6,7,8] and Diego Vescovi[9,10,11]

[1]*Theoretisch-Physikalisches Institut, Friedrich-Schiller-Universität Jena, Fröbelstieg 1, D-07743 Jena, Germany*
[2]*Dipartimento di Fisica, Universitá di Trento, Via Sommarive 14, I-38123 Trento, Italy*
[3]*INFN-TIFPA, Trento Institute for Fundamental Physics and Applications, via Sommarive 14, I-38123 Trento, Italy*
[4]*Dipartimento di Fisica "Enrico Fermi", Universitá di Pisa, Largo B. Pontecorvo 14, I-56127 Pisa, Italy*
[5]*INFN, Sezione di Pisa, Largo B. Pontecorvo 14, I-56127 Pisa, Italy*
[6]*Institute for Gravitation & the Cosmos, The Pennsylvania State University, University Park, PA 16802, USA*
[7]*Department of Physics, The Pennsylvania State University, University Park, PA 16802, USA*
[8]*Department of Astronomy & Astrophysics, The Pennsylvania State University, University Park, PA 16802, USA*
[9]*Gran Sasso Science Institute, Viale F. Crispi 7, I-67100 L'Aquila, Italy*
[10]*INFN, Sezione di Perugia, Via A. Pascoli 23, I-06123 Perugia, Italy*
[11]*INAF, Observatory of Abruzzo, Via M. Maggini, I-64100, Teramo, Italy*

Accepted 2021 May 3. Received 2021 May 3; in original form 2021 January 7

ABSTRACT

The joint detection of the gravitational wave GW170817, of the short γ-ray burst GRB170817A and of the kilonova AT2017gfo, generated by the the binary neutron star (NS) merger observed on 2017 August 17, is a milestone in multimessenger astronomy and provides new constraints on the NS equation of state. We perform Bayesian inference and model selection on AT2017gfo using semi-analytical, multicomponents models that also account for non-spherical ejecta. Observational data favour anisotropic geometries to spherically symmetric profiles, with a log-Bayes' factor of $\sim 10^4$, and favour multicomponent models against single-component ones. The best-fitting model is an anisotropic three-component composed of dynamical ejecta plus neutrino and viscous winds. Using the dynamical ejecta parameters inferred from the best-fitting model and numerical–relativity relations connecting the ejecta properties to the binary properties, we constrain the binary mass ratio to $q < 1.54$ and the reduced tidal parameter to $120 < \tilde{\Lambda} < 1110$. Finally, we combine the predictions from AT2017gfo with those from GW170817, constraining the radius of a NS of 1.4 $M_\odot$ to 12.2 ± 0.5 km (1σ level). This prediction could be further strengthened by improving kilonova models with numerical-relativity information.

Key words: equation of state – methods: data analysis – neutron star mergers.

1 INTRODUCTION

On 2017 August 17, the ground-based interferometers of *LIGO* and *Virgo* (Aasi et al. 2015; Acernese et al. 2015; Abbott et al. 2018a) detected the first gravitational-wave (GW) signal coming from a binary neutron star (BNS) merger, known as GW170817 (Abbott et al. 2017a). GW170817 was followed by a short gamma-ray burst (GRB) GRB170817A (Abbott et al. 2017c; Savchenko et al. 2017), which reached the space observatories Fermi (Ajello et al. 2016) and INTEGRAL (Winkler et al. 2011) ∼1.7 s after coalescence time. 11 h later, several telescopes started to collect photometric and spectroscopical data from AT2017gfo, an unprecedented electromagnetic (EM) kilonova transient (Chornock et al. 2017; Coulter et al. 2017; Cowperthwaite et al. 2017; Nicholl et al. 2017; Pian et al. 2017; Smartt et al. 2017; Tanaka et al. 2017; Tanvir et al. 2017; Valenti et al. 2017) coming from a coincident region of the sky. Kilonovae (kNe) are quasi-thermal EM emissions interpreted as distinctive signature of *r*-process nucleosynthesis in the neutron-rich matter ejected from the merger and from the subsequent BNS remnant evolution (Kasen et al. 2017; Smartt et al. 2017; Rosswog et al. 2018; Kawaguchi, Shibata & Tanaka 2020 Metzger 2020). The follow up of the source lasted for more than a month and included also non-thermal emission from the GRB170817A afterglow (e.g. Nynka et al. 2018; Hajela et al. 2019).

The combined observation of GW170817, GRB170817A, and AT2017gfo decreed the dawn of multimessenger astronomy with compact binaries (Abbott et al. 2017b). From these multimessenger observations, it is possible to infer unique information on the unknown equation of state (EOS) of neutron star (NS) matter (e.g. Bauswein et al. 2017; Margalit & Metzger 2017; Radice et al. 2017; Dietrich et al. 2018; Radice et al. 2018b). Indeed, the EOS determines the tidal polarizability parameters that describe tidal interactions during the inspiral-merger and characterize the GW signal (Damour, Nagar & Villain 2012; Bernuzzi et al. 2014). It also determines the outcome of BNS mergers (e.g. Shibata, Taniguchi & Uryu 2005; Bernuzzi et al. 2015a, 2020) and the subsequent post-merger GW

★ E-mail: matteo.breschi@uni-jena.de

signal from the remnant (e.g. Bauswein, Stergioulas & Janka 2014; Bernuzzi, Dietrich & Nagar 2015b; Breschi et al. 2019; Zappa et al. 2019; Agathos et al. 2020). At the same time, the amount of mass, the velocity, and the composition of the ejecta are also strongly dependent on the EOS, which has an imprint on the kN signature e.g. (Bauswein, Goriely & Janka 2013; Hotokezaka et al. 2013; Radice et al. 2018a,d).

The spectrum of AT2017gfo was recorded from ultraviolet (UV) to near-infrared (NIR) frequencies (e.g. Pian et al. 2017; Nakar et al. 2018), and the observations showed several characteristic features. At early stages, the kN was very bright and its spectrum peaked in the blue band 1 d after the merger (blue kN). After that, the peak of the spectrum moved towards larger wavelengths, peaking at NIR frequencies between 5 and 7 d after merger (red kN). Minimal models that can explain these features require more than one component. In particular, minimal-fitting models assume spherical symmetry and include a lathanide-rich ejecta responsible for the red kN, typically interpreted as dynamical ejecta, and another ejecta with material partially reprocessed by weak interaction, responsible for the blue component (e.g. Villar et al. 2017b). Numerical relativity (NR) simulations show that the geometry profiles of the ejecta are not always spherically symmetric and their distributions are not homogeneous (Perego, Radice & Bernuzzi 2017a). Moreover, NR simulations also indicate the presence of multiple ejecta components, from the dynamical to the disc winds ejecta (Metzger & Fernández 2014; Perego et al. 2014; Rosswog et al. 2014; Fernández et al. 2015; Nedora et al. 2019). Therefore, this information has to be taken into account during the inference of the kN properties.

The modelling of kNe is a challenging problem due to the complexity of the underlying physics, which is affected by a diverse interactions and scales (see Metzger 2020, and references therein). Together with the choice of ejecta profiles, the lack of a reliable description of the radiation transport is a relevant source of uncertainties in the modelling of kNe, due to the incomplete knowledge on the thermalization processes (Korobkin et al. 2012; Barnes et al. 2016) and on the energy-dependent photon opacities in *r*-process matter (Even et al. 2020; Tanaka et al. 2020). Current kN models often use either simplistic ejecta profiles or simplistic radiation schemes (e.g. Grossman et al. 2014; Coughlin et al. 2017; Perego et al. 2017a; Villar et al. 2017b). Given the challenges and uncertainties associated to the theoretical prediction of kN features, Bayesian inference and model selection of the observational data can provide important insights on physical processes hidden in the kN signature.

In this work, we explore model selection in geometrical and ejecta properties using simplified light-curve (LC) models, which none the less capture the key features of the problem. The inference results are then employed to derive constraints on the NS EOS. In Section 2, we describe the semi-analytical model and the ejecta components used in our analysis. In Section 3, we recall the Bayesian framework for model selection, highlighting the choices of the relevant statistical quantities, such as likelihood function and prior distributions. In Section 4, we discuss the inference on AT2017gfo, critically examining the posterior samples in light of targeted NR simulations (Nedora et al. 2019; Perego, Bernuzzi & Radice 2019; Bernuzzi et al. 2020; Endrizzi et al. 2020; Nedora et al. 2021) and previous analyses. In Section 5, we discuss new constraints on the NS EOS focusing first on mass ratio and reduced tidal parameter for the source of GW170817, and then on the NS radius $R_{1.4}$. We conclude in Section 6.

2 KILONOVA MODEL

In this section, we first summarize basic analytical results and scaling relations that characterize the kN emission, and then describe in detail the models we employ for the ejecta components and LC calculations.

2.1 Basic features

Let us consider a shell of ejected matter characterized by a mass density ϱ, with total mass m and grey opacity κ (mean cross-section per unit mass). The shell is in homologous expansion symmetrically with respect to the equatorial plane at velocity v, such that its mean radius is $R \sim vt$ after a time t following the merger. Matter opacity to EM radiation can be expressed in terms of the optical depth, τ, which is estimated as $\tau \simeq \varrho\kappa R$. After the BNS collision, when matter becomes unbound and *r*-process nucleosynthesis occurs, the ejecta are extremely hot, $T \sim 10^9$ K (e.g. de Jesús Mendoza-Temis et al. 2015; Wu et al. 2016; Perego et al. 2019). However, at early times the thermal energy is not dissipated efficiently since the environment is optically thick ($\tau \gg 1$) and photons diffuse out only on the diffusion time-scale until they reach the photosphere ($\tau = 2/3$). As the outflow expands, its density drops ($\rho \propto t^{-3}$) and the optical depth decreases.

The key concept behind kNe is that photons can contribute to the EM emission at a given time t if they diffuse on a time-scale comparable to the expansion time-scales, i.e. if they escape from the shells outside $R_{\rm diff}$, where $R_{\rm diff}$ is the radius at which the diffusion time $t_{\rm diff} \simeq R\tau/c$ equals the dynamical time t (Piran, Nakar & Rosswog 2013; Grossman et al. 2014; Metzger 2020). In the previous expression, c is the speed of light. Since $t_{\rm diff} \propto t^{-1}$, a larger and larger portion of the ejecta becomes transparent with time. The luminosity peak of the kN occurs when the bulk of matter that composes the shell becomes transparent. As first approximation, the characteristic time-scale at which the LC peaks is commonly estimated (Arnett 1982) as:

$$t_{\rm peak} = \sqrt{\frac{3m\kappa}{4\pi\beta vc}}, \tag{1}$$

where the dimensionless factor β depends on the density profile of the ejecta. For a spherical symmetric, homologously expanding ejecta ($\beta \simeq 3$) with mass $m = 10^{-2}\ {\rm M}_\odot$, velocity $v = 0.1\ c$ and opacity in the range $\kappa \simeq 1{-}50\ {\rm cm^2\ g^{-1}}$, which are typical values respectively for lanthanide-free and for lanthanide-rich matter (Roberts et al. 2011; Kasen, Badnell & Barnes 2013), equation (1) predicts a characteristic $t_{\rm peak}$ in the range 1–10 d (Abbott et al. 2017d).

In the absence of a heat source, matter would simply cool down through adiabatic expansion. However, the ejected material is continuously heated by the radioactive decays of the *r*-process yields, which provide a time-dependent heating rate of nuclear origin. An additional time dependence is introduced by the thermalization efficiency, i.e. the efficiency at which this nuclear energy, released in the form of supra-thermal particles (electrons, daughter nuclei, photons, and neutrinos), thermalizes within the expanding ejecta (see e.g. Korobkin et al. 2012; Metzger & Berger 2012; Barnes et al. 2016; Hotokezaka, Beniamini & Piran 2018).

2.2 Light curves

The kN LCs in our work are computed using the multicomponent, anisotropic semi-analytical `MKN` model first introduced in ref. (Perego et al. 2017a) and largely based on the kN models presented in refs. (Grossman et al. 2014) and (Martin et al. 2015; see also Barbieri et al. (2019)). The ejecta are either spherical or

axisymmetric with respect to the rotational axis of the remnant, and symmetric with respect to the equatorial plane. The viewing angle ι is measured as the angle between the rotational axis and the line of sight of the observer.

For each component, the ejected material is described through the angular distribution of its ejected mass, m, rms radial velocity, $v_{\rm rms}$, and opacity, κ. In axisymmetric models, the latter quantities are functions of the polar angle θ, measured from the rotational axis and discretized in $N_\theta = 30$ angular bins evenly spaced in $\cos\theta$. Additionally, within each ray, matter is radially distributed with a stationary profile in velocity space, $\xi(v)$ such that $\xi(v) \propto (1 - (v/v_{\rm max})^2)^3$, where $\xi(v){\rm d}v$ is the matter contained in an infinitesimal layer of speed $[v, v + {\rm d}v]$, and $v_{\rm max} = v_{\rm max}(v_{\rm rms})$ is the maximum velocity at the outermost edge of the component. The characteristic quantities ϱ, v, and κ are then evaluated for every bin according to the assumed input profiles. For every bin, we estimate the emitted luminosity using the radial model described in ref. (Perego et al. 2017a) and in section 4 of ref. (Barbieri et al. 2020; see also Barbieri et al. 2019). In particular, the model assumes that the luminosity is emitted as thermal radiation from the photosphere (of radial coordinate $R_{\rm ph}$), and the luminosity and the photospheric surface determine the effective emission temperature, $T_{\rm eff}$ through the Stefan–Boltzmann law. We expect this assumption to be well verified at early times (with a few days after merger), while deviations from it are expected to become more and more relevant for increasing time.

The time-dependent nuclear heating rate $\epsilon_{\rm nuc}$ entering these calculations is approximated by an analytic fitting formula, derived from detailed nucleosynthesis calculations (Korobkin et al. 2012),

$$\epsilon_{\rm nuc}(t) = \epsilon_0 \frac{\epsilon_{\rm th}(t)}{0.5} \epsilon_{\rm nr}(t) \left[\frac{1}{2} - \frac{1}{\pi} \arctan\left(\frac{t - t_0}{\sigma}\right)\right]^\alpha, \tag{2}$$

where $\sigma = 0.11$ s, $t_0 = 1.3$ s, $\alpha = 1.3$ and $\epsilon_{\rm th}(t)$ is the thermalization efficiency tabulated according to ref. (Barnes et al. 2016). The heating factor $\epsilon_{\rm nr}(t)$ is introduced as in ref. (Perego et al. 2017a) to roughly improve the behaviour of equation (2) in the regime of mildly neutron-rich matter (characterized by an initial electron fraction $Y_e \gtrsim 0.25$), (see e.g. Martin et al. 2015):

$$\epsilon_{\rm nr}(t, \kappa) = [1 - w(\kappa)] + w(\kappa)\, \epsilon_{Y_e}(t), \tag{3}$$

where $w(\kappa)$ is a logarithmic smooth clump function such that $w(\kappa < 1\ {\rm cm^2\ g^{-1}}) = 1$ and $w(\kappa > 10\ {\rm cm^2\ g^{-1}}) = 0$ and the factor $\epsilon_{Y_e}(t)$ encodes the dependence on Y_e: if $Y_e < 0.25$, then $\epsilon_{Y_e}(t) = 1$, otherwise, when $Y_e \geq 0.25$,

$$\epsilon_{Y_e}(t) = \epsilon_{\rm min} + \epsilon_{\rm max} \left[1 + e^{4(t/t_\epsilon - 1)}\right]^{-1}, \tag{4}$$

where $t_\epsilon = 1$ d, $\epsilon_{\rm min} = 0.5$, and $\epsilon_{\rm max} = 2.5$.

Furthermore, in order to improve the description in the high-frequency bands (i.e. V, U, B, and g) within the time-scale of the kilonova emission, and following ref. (Villar et al. 2017a), we introduce a floor temperature, i.e. a minimum value for $T_{\rm eff}$. This is physically related to the drop in opacity due to the full recombination of the free electrons occurring when for the matter temperature drops below $T_{\rm floor}$ (Kasen et al. 2017; Kasen & Barnes 2019). Under these assumptions, the condition $T_{\rm eff} = T_{\rm floor}$ becomes a good tracker for the photosphere location. Since kNe are powered by the radioactive decay of different blends of atomic species, we introduce in our model two floor temperatures, $T^{\rm Ni}_{\rm floor}$ and $T^{\rm LA}_{\rm floor}$, which characterize, respectively, the recombination temperature of lanthanide-free and of lanthanide-rich ejecta.

Eventually, the emissions coming from the different rays are combined to obtain the spectral flux at the observer location:

$$F_\nu(\mathbf{n}, t) = \int_{\mathbf{n}_\Omega \cdot \mathbf{n} > 0} \left(\frac{R_{\rm ph}(\Omega, t)}{D_{\rm L}}\right)^2 B_\nu(T_{\rm eff}(\Omega, t))\, \mathbf{n} \cdot {\rm d}\mathbf{\Omega} \tag{5}$$

where $\mathbf{n}$ is the unitary vector along the line of sight, $\mathbf{n}_\Omega$ is the unitary vector spanning the solid angle Ω, $D_{\rm L}$ is the luminosity distance, $R_{\rm ph}$ is the local radial coordinate of the photospheric surface, and $B_\nu(T_{\rm eff})$ is the spectral radiance at frequency ν for a surface of temperature $T_{\rm eff}$. Lastly, from equation (5), it is possible to compute the apparent AB magnitude ${\rm mag}_b$ in a given photometric band b as:

$${\rm mag}_b(\mathbf{n}, t) = -2.5 \log_{10}\left(F_{\nu_b}(\mathbf{n}, t)\right) - 48.6, \tag{6}$$

where ν_b is the effective central frequency of band b.

2.3 Multicomponent model

In order to describe the different properties of AT2017gfo, it is necessary to appeal to a multicomponent structure for the ejecta producing the kN. Different components are characterized by different sets of intrinsic parameters, m, $v_{\rm rms}$, and κ and by their angular distributions with respect to θ.

Given the angular profiles of the characteristic parameters, the physical luminosity produced by each component inside a ray is computed by using the model outlined in the previous section. Then, the total bolometric luminosity of the ray is given by the sum of the single contributions, i.e. $L(t) = \sum_k L^{(k)}(t)$ where k runs over the components. The outermost photosphere is the one that determines the thermal spectrum of the emission. Once $R_{\rm ph}$ and $T_{\rm eff}$ have been determined, the spectral flux and the AB magnitudes are computed according to equations (5 and 6).

We perform the analysis using two different assumptions on the profiles of the source. Initially, we impose completely isotropic profiles for every parameter of every ejecta component. These cases are labelled as isotropic, '*ISO*'. Subsequently, we introduce angular profiles as functions of the polar angle for the mass and opacity parameters, while we keep $v_{\rm rms}$ always isotropic. This second case is labelled as anisotropic, '*ANI*''. In parallel, we explore models with a different number of components. We always assume the presence of the dynamical ejecta, while we add to them one or two qualitatively different disc-wind ejecta components.

In the following paragraphs, we describe the physical assumptions on each component and the choice of the prior distributions (see Table 1). Fig. 1 shows a graphical representation of the employed ejecta components.

We conclude this section by recalling that the main motivation behind the usage of the semi-analytic model presented above is the optimal compromise between its robustness and adaptability, essential to model the non-trivial structure of the ejecta, and the reduced computational costs, necessary to perform parameter estimation studies. However, it has been showed that simplified models that avoid the solution of the radiation transport problem can suffer from systematic uncertainties (Wollaeger et al. 2018). In particular, the analytical model presented in (Grossman et al. 2014), on which ours is based, produces significantly lower LCs. The comparison with observed kN LCs and more detailed kN models showed how larger nuclear heating rates ϵ_0 systematically reduce this discrepancy.

2.3.1 *Dynamical ejecta (D)*

The BNS collision ejects unbound matter on the dynamical time-scale, whose properties strongly depend on the total mass of the

Table 1. List of intrinsic and extrinsic parameters involved in the analysis and the respective prior bounds for the cases of anisotropic geometry. For isotropic geometry cases, the bounds are identical except for the opacity κ of dynamical component (D), where the low-latitude and high-latitude bounds are joined together.

Intrinsic ejecta parameters $\boldsymbol{\theta}_{\rm ej}^{\rm (D,V,N)}$					
Comp.	m [$10^{-2}\,{\rm M}_\odot$]	$v_{\rm rms}$ [c]	$\kappa_{\rm high}$	$\kappa_{\rm low}$ [$\rm cm^2\,g^{-1}$]	$\theta_{\rm step}$ [rad]
D	[0.1, 10]	[0.15, 0.333]	[0.1, 5]	[5, 30]	$\pi/4$
N	[0.01, 0.75]	[0.05, 0.15]	[0.01, 5]		$\pi/3$
V	[1, 20]	[0.001, 0.1]	[0.01, 30]		–
Intrinsic global parameter $\boldsymbol{\theta}_{\rm glob}$					
$T_{\rm floor}^{\rm Ni}$	[K]		[500, 8000]		
$T_{\rm floor}^{\rm LA}$	[K]		[500, 8000]		
ϵ_0	[$\rm erg\,g^{-1}\,s^{-1}$]		$[2\times10^{17}, 5\times10^{19}]$		
Extrinsic parameters $\boldsymbol{\theta}_{\rm ext}$					
D_L	[Mpc]		[15, 50]		
ι	[deg]		[0, 70]		

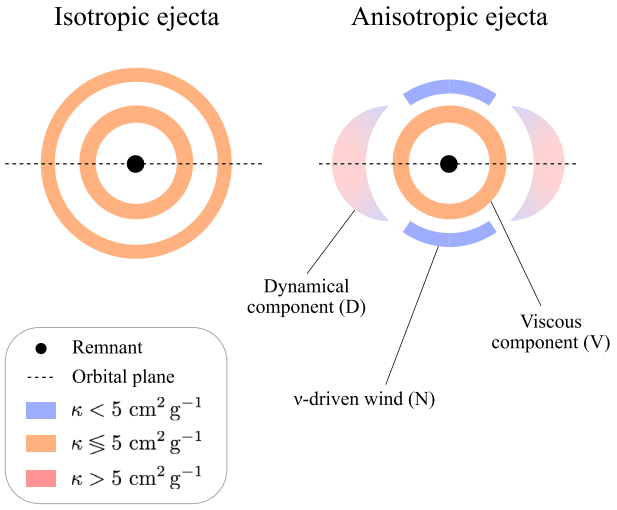

Figure 1. Graphic representation of the analyzed ejecta profiles for isotropic and anisotropic cases from an azimuthal perspective and for a fixed moment of time. The black dot represents the remnant and the dashed line is the projected orbital plane of the binary. The shadowed areas describe the ejecta profiles: the shape characterizes the mass distribution, while the colours refer to the prior assumptions on the opacity parameter. In particular, blue regions denote opacities lower than 5 $\rm cm^2\,g^{-1}$, red regions refer to opacities greater than 5 $\rm cm^2\,g^{-1}$, and oranges areas indicate a broadly distributed opacity. All shells are isotropically expanding with a constant velocity.

BNS, on the mass ratio and on the EOS (e.g. Bauswein et al. 2013; Hotokezaka et al. 2013; Rosswog, Piran & Nakar 2013; Radice et al. 2016; Bovard et al. 2017; Radice et al. 2018c,d). This ejection is due to tidal torques and shocks developing at the contact interface between the merging stars, when matter is squeezed out by hydrodynamical processes (Oechslin, Janka & Marek 2007; Hotokezaka et al. 2013). The expansion of this ejecta component has a velocity of roughly $v_{\rm rms}\sim 0.2\,c$. Moreover, this phenomenon generates a distribution of ejected mass denser in the regions across the orbital plane with respect to the region along its orthogonal axis, characterized by larger opacities at lower latitudes. In particular, neutrino irradiation (if significant), increases the ejecta Y_e and prevents the formation of lanthanides. For the anisotropic analyses, the mass profile is taken to be $\varrho(\theta)\propto\sin\theta$, and the opacity profile is take as a step function in the polar angle characterized by the parameters $(\kappa_{\rm low}, \kappa_{\rm high})$, respectively for low and high latitudes, with a step angle $\theta_{\rm step}=\pi/4$ (see Section 3.3). In terms of emitted LC, the described ejecta is characterized by a red equatorial component and a blue contribution at higher latitudes.

2.3.2 *Neutrino-driven wind (N)*

Simulations of the remnant evolution in the aftermath of a BNS merger reveal the presence of other ejection mechanisms happening over the thermal and viscous evolution time-scales (e.g. Metzger, Piro & Quataert 2008; Fernández & Metzger 2013; Perego et al. 2014; Perego, Yasin & Arcones 2017b; Decoene et al. 2020). If the ejection happens while the remnant is still a relevant source of neutrinos, neutrino irradiation has enough time to increase Y_e above 0.25, preventing full r-process nucleosynthesis, especially close to the polar axis. Detailed simulations (Perego et al. 2014; Martin et al. 2015; Fujibayashi et al. 2018; Fujibayashi et al. 2020) show that a relatively small fraction of the expelled disc contributes to this component and its velocity is expected to be $v_{\rm rms}\lesssim 0.1c$. For anisotropic analyses, the mass profile is taken to be uniform in the range $\theta\in[0, \pi/3]$ and negligible otherwise, while the opacity profile is taken as a step function in the polar angle, with a step angle $\theta_{\rm step}=\pi/3$.

2.3.3 *Disc's viscous ejecta (V)*

In addition to neutrinos, viscous torques of dynamical and magnetic origin can unbind matter from the disc around massive NSs or black holes (Metzger et al. 2010; Metzger & Fernández 2014; Just, Obergaulinger & Janka 2015). This viscous component is expected to unbound a large fraction of the disc matter on longer time-scale, reaching $m\lesssim 10^{-1}\,{\rm M}_\odot$, with a relatively low velocity, $v_{\rm rms}\lesssim 0.05c$. The corresponding ejecta are more uniformly distributed over the polar angle than the dynamical ejecta and the ν-driven wind ejecta. The presence or the lack of a massive NS in the centre can influence the Y_e of these ejecta. Then, all angular profiles are assumed to be isotropic for this component (Wu et al. 2016; Siegel & Metzger 2018).

3 METHOD

In this section, we recall the basic concepts of model selection as they are stated in the Bayesian theory of probability. Then, we describe the statistical technique used for the computations of the Bayes' factors. As convention, the symbol 'log ' denotes the natural logarithm while a logarithm to a different base is explicitly written when it is used.

3.1 Model selection

Given some data d and a model H (hypothesis) described by a set of parameters $\boldsymbol{\theta}$, the posterior probability is given by the Bayes' theorem:

$$p(\boldsymbol{\theta}|d,H)=\frac{p(d|\boldsymbol{\theta},H)\,p(\boldsymbol{\theta}|H)}{p(d|H)}, \tag{7}$$

where $p(d|\boldsymbol{\theta},H)$ is the likelihood function, $p(\boldsymbol{\theta}|H)$ is the prior probability assigned to the parameters, and $p(d|H)$ is the evidence.

The latter value plays the role of normalization constant and it can be computed by marginalizing the likelihood function,

$$p(d|H) = \int_{\Theta} p(d|\boldsymbol{\theta}, H)\, p(\boldsymbol{\theta}|H) \mathrm{d}\boldsymbol{\theta}, \tag{8}$$

where the integral is computed over the entire parameters' space Θ.

In the framework of Bayesian theory of probability, we can compare two models, say A and B, by computing the ratios of the respective posterior probabilities, also known as *Bayes' factor*,

$$\mathcal{B}^A_B = \frac{p(A|d, H_A)}{p(B|d, H_B)}. \tag{9}$$

Using equation (7) we get:

$$\mathcal{B}^A_B = \frac{p(d|A, H_A)}{p(d|B, H_B)} \frac{p(A|H_A)}{p(B|H_B)} = \frac{p(d|A, H_A)}{p(d|B, H_B)}, \tag{10}$$

where we assumed that the data do not depend on the different hypothesis and that different models are equally likely *a priori*, i.e. $p(A|H_A) = p(B|H_B)$. Now suppose that the two models A, B are respectively described by two sets of parameters $\boldsymbol{\theta}_A, \boldsymbol{\theta}_B$. Using the marginalization rule we can write:

$$p(d|I, H_I) = \int_{\Theta_I} p(d|\boldsymbol{\theta}_I, I, H_I)\, p(\boldsymbol{\theta}_I|I, H_I)\, \mathrm{d}\boldsymbol{\theta}_I, \tag{11}$$

for $I = A, B$. The integral in equation (11) represents the evidence computed for the hypotheses $H'_I = \{H_I, I\}$, for $I = A, B$ (i.e. the involved model becomes part of the background hypothesis). Then, we obtain that the Bayes' factor $\mathcal{B}^A_B$ can be computed as

$$\mathcal{B}^A_B = \frac{p(d|H'_A)}{p(d|H'_B)}. \tag{12}$$

From the previous results, we understand that if $\mathcal{B}^A_B > 1$ then the model A will be favoured by the data, vice versa if $\mathcal{B}^A_B < 1$. It is important to observe that the Bayes' factor implicitly takes into account the so called Occam's razor, i.e. if two models are both able to capture the features of the data, then the one with lower number of parameters will be favoured (Sivia & Skilling 2006). In our analysis, this is a crucial point since different models have different numbers of parameters.

3.2 Nested sampling

In a realistic scenario, the form of the likelihood function is analytically indeterminable and the parameter space has a non-trivial number of dimensions. For these reasons, the estimation of equation (11) is performed resorting to statistical computational techniques: we employ the nested sampling Bayesian technique introduced in ref. (Skilling 2006) and designed to compute the evidence and explore the full parameter space. The uncertainties associated with the evidence estimations are computed according to ref. (Skilling 2006) and increasing the result by one order of magnitude, in order to conservatively take into account systematics. The latter are expected since the model considered for our analyses (as many others) cannot capture all the physics processes involved in kNe, and it suffers of large uncertainties in the atomic physics and radiative processes implementation.

We perform inference with CPNEST (Del Pozzo & Veitch 2021), a parallelized nested sampling implementation. We use 1024 live points and, for every step, we set a maximum number of 2048 Markov chain Monte Carlo (MCMC) iterations for the exploration of the parameter space. The proposal step method used in the MCMC is the same as the one implemented as default in CPNEST software. It corresponds to a cycle over four different proposal methods: a random-walk step (Goodman & Weare 2010), a stretch move (Goodman & Weare 2010), a differential evolution method (Nelson, Ford & Payne 2013), and a proposal based on the eigenvectors of the covariance matrix of the ensemble samples, as implemented in ref. (Veitch et al. 2015).

3.3 Choice of priors

In our analysis, we assume the sky position of the source to be known and the time of coalesce to be the same of the trigger time of GW170817 (Abbott et al. 2017a). Furthermore, we do not take into account the redshift contribution, given the larger systematic uncertainties in the model. We employ the parameters shown in Table 1, which can be divided in three subsets: the intrinsic ejecta parameters $\boldsymbol{\theta}^{(\mathrm{D,V,N})}_{\mathrm{ej}}$, the intrinsic global parameters $\boldsymbol{\theta}_{\mathrm{glob}}$, and the extrinsic parameters $\boldsymbol{\theta}_{\mathrm{ext}}$.

The intrinsic ejecta parameters, $\boldsymbol{\theta}^{(k)}_{\mathrm{ej}}$ for $k = \mathrm{D, V, N}$, characterize the properties of each ejecta component and they are the amount of ejected mass, m, the rms velocity of the fluid, v_{rms}, and their grey opacity, κ. Under the assumption of isotropic geometry, the intrinsic ejecta parameters $\boldsymbol{\theta}^{(k)}_{\mathrm{ej}}$ are defined by a single value for every shell, i.e. a single number characterizes the entire profile of the parameter of interest, since it is spherically symmetric. However, for anisotropic cases, we have to introduce more than one independent parameters to describe an angular profile for a specific variable: this is the case of the opacity parameter of the dynamical component, where the profile is chosen as step functions characterized by two different parameters, κ_{low} and κ_{high}, respectively at low and high latitudes. In such a cases, the angle θ_{step} is introduced to denote the angle at which the profile changes value, as mentioned in Section 2.3.

The intrinsic global parameters, $\boldsymbol{\theta}_{\mathrm{glob}}$, represent the properties of the source common to every component, such as the floor temperatures, $T^{\mathrm{Ni}}_{\mathrm{floor}}$ and $T^{\mathrm{LA}}_{\mathrm{floor}}$, and the heating rate constant ϵ_0. In principle, the latter is a universal property which defines the nuclear heating rate as expressed in equation (2). The whole set of intrinsic parameters, $\boldsymbol{\theta}_{\mathrm{glob}}$ and $\boldsymbol{\theta}^{(k)}_{\mathrm{ej}}$, determines the physical dynamics of the system and therefore they determine the properties of the kN emission, irrespectively of the observer location.

The extrinsic parameters, $\boldsymbol{\theta}_{\mathrm{ext}}$, are the luminosity distance of the source, D_{L} and the viewing angle ι. These parameters do not depend on the physical properties of the source and they are related with the observed signal through geometrical argumentation.

The prior distributions for all the parameters are taken uniform in their bounds, except for the followings. For the extrinsic parameters $\boldsymbol{\theta}_{\mathrm{ext}} = \{D_L, \iota\}$, we set the priors equal to the marginalized posterior distributions coming from the low-spin-prior measurement of GW170817 (Abbott et al. 2019b); For the heating rate factor ϵ_0, we use a uniform prior distribution in $\log \epsilon_0$, i.e. $p(\epsilon_0|H) \propto \epsilon_0{}^{-1}$, since this parameter strongly affects the LC and it is free to vary in a wide range. Moreover, we adopt a prior range according with the estimation given in ref. (Korobkin et al. 2012). Table 1 shows the prior bounds used for the analysis of the anisotropic cases. For the isotropic studies, the bounds are identical except for the opacity κ of dynamical component, where the low-latitude and high-latitude bounds are joined together.

3.4 Likelihood function

The data $\{d_{b,i} \pm \sigma_{b,i}\}$ are the apparent magnitudes observed from AT2017gfo, with their standard deviations. They have been collected from (Villar et al. 2017b), where all the precise reference to the original works and to the data reduction techniques can be found. The index b runs over all considered photometric bands, covering a

wide photometric range from the UV to the NIR, while for each band b the index i runs over the corresponding sequence of N_b temporal observations. Additionally, the magnitudes have been corrected for Galactic extinction (Cardelli, Clayton & Mathis 1989). We introduce a Gaussian likelihood function in the apparent magnitudes with mean and variance, $d_{b,i}$, $\sigma^2_{b,i}$, from the observations of AT2017gfo,

$$\log p(\boldsymbol{\theta}|d, H) \propto -\frac{1}{2}\sum_{b}\sum_{i=1}^{N_b}\frac{\left|d_{b,i}-\mathrm{mag}_{b,i}(\boldsymbol{\theta})\right|^2}{\sigma^2_{b,i}}, \tag{13}$$

where $\mathrm{mag}_{b,i}(\boldsymbol{\theta})$ are the magnitudes generated by the LC model, of Section 2, which encodes the dependency on the parameters $\boldsymbol{\theta}$, for every band b at different times i. The likelihood definition equation (13) is in accordance with the residuals introduced in Ref. (Perego et al. 2017a) and it takes into account the uncertainties due to possible technical issues of the instruments and generic non-stationary contributions, providing a good characterization of the noise.[1]For both geometric configurations, isotropic (*ISO*) and anisotropic (*ANI*), we perform Bayesian analyses using different combinations of components, testing the capability to fit the data.

4 RESULTS

In this section, we present the results gathered from the Bayesian analysis. In Section 4.1, we describe the capability of the synthetic LCs to fit the observed data. After that, in Section 4.2, we discuss the estimated evidence inferring the preferred model. Finally, in Section 4.3, we discuss the interpretation of the recovered posterior distributions.

4.1 Light curves

Fig. 2 shows the LCs computed from the recovered maximum-likelihood parameters for each discussed model. The estimated LCs are compared with AT2017gfo data for six representative photometric bands. Moreover, Fig. 3 shows the uncertainties associated with the estimated LCs, computed over the recovered posterior samples, for each considered model. Generally, the errors associated with the near-UV (NUV) magnitudes are larger compared with the other bands, reflecting the lower number of data points in this photometric region. Furthermore, none of the considered model is able to fully capture the trend described by the observed data in the Ks band for time larger then 10 d, within the provided prior bounds. This is expected from the simplified treatment of the radiation transport and the approximated heating rate in our models.

The isotropic models (*ISO*-D and *ISO*-DV) give a good fitting to the data for early times and their LCs capture the general trends of the data. However, for times larger than ∼8 d, these models do not capture all the features of the data within the provided prior bounds. This inaccuracy is particularly evident in the NIR, where the LCs predicted by the *ISO*-D and the *ISO*-DV models do not recover the correct slopes of the data.

The anisotropic single-component case, *ANI*-D, is apt at adapting the model to the different features present in the data, even for large time-scales. However, it overestimates the kN emission in the blue band. This inconsistency could be reduced allowing the high-latitude opacity parameter κ_{high} to lower values. Regarding the anisotropic two-components models, the *ANI*-VN gives a good fitting for early times, but the model largely underestimates the data at times $\gtrsim 5$ d. This is due to the absence of a fast blue component. The anisotropic *ANI*-DV model gives LCs similar to *ANI*-D except for a slight excess of power for time $\gtrsim 10$ d, especially in the NIR region, i.e. z, K, and K_s bands. This behaviour could be mitigated by reducing the lower bound on the $T^{\mathrm{LA}}_{\mathrm{floor}}$ parameter. However, it could also indicate a significant deviation from the black-body emission adopted in our model at late times. Furthermore, the *ANI*-DV model overshoots the data in the NUV, as it is for the respective single-component case *ANI*-D. This can be explained looking at the recovered value of dynamical ejected mass, which exceeds theoretical expectations estimated from NR simulations (Nedora et al. 2019; Perego et al. 2019; Bernuzzi et al. 2020; Endrizzi et al. 2020; Nedora et al. 2021; see Section 4.3.4). Similar considerations hold for the anisotropic three-component case *ANI*-DVN. However, the uncertainties on the estimated LCs for this model are narrower with respect to the ones obtained from the *ANI*-DV, corresponding to an improvement in the capability of constraining the measurement. The main improvement of the three-component *ANI*-DVN model over the two-component *ANI*-DV model lies in its ability to better fit early-times data due to the inclusion of a third component.

4.2 Evidences

The logarithmic evidences estimated for the considered models are shown in Table 2. The evidence increases with the number of models' components. This is consistent with the hierarchy observed in the LC residuals, and the better match to the data for multicomponent models. The only exception is the *ANI*-NV case, for which the features of the data at late times are not well captured due to the absence of a fast equatorial component. Furthermore, for a fixed number of components, the anisotropic geometries are always favoured with respect to isotropic geometries, with a $\log \mathcal{B}^{\mathrm{ANI}}_{\mathrm{ISO}}$ of the order of 10^4. The preferred model among the considered cases is the anisotropic three-component, in agreement with previous findings, e.g. (Cowperthwaite et al. 2017; Perego et al. 2017a; Villar et al. 2017b).

4.3 Posterior distributions

In the following paragraphs, we discuss the properties of the posterior distributions for each model and their physical interpretation. Tables 3 and 4 show the mean values of the parameters, and their 90 per cent credible regions, extracted from the recovered posterior distributions. A general fact is that the marginalized posterior for the ejected mass of the viscous component is always constrained against the lower bound 10^{-2} $\mathrm{M}_{\odot}$, when this component is involved. Moreover, for the majority of the analyses, the distance parameter is biased towards larger values, inconsistently with the estimates from ref. (Abbott et al. 2017a,b), and the heating rate parameter ϵ_0 is generally overestimated comparing with the estimates from nuclear calculations (Korobkin et al. 2012; Barnes et al. 2016; Kasen & Barnes 2019; Barnes et al. 2020; Zhu et al. 2021). This behaviour can be explained from equations (2, 5, and 6): D_{L} and ϵ_0 are largely degenerate and both concur to determine the brightness of the observed LCs. Thus, the correlations between these parameters induce biases in the recovered values. The physical explanation of this effect can be motivated with the poor characterization of the model in the NIR bands: this lack of knowledge generates a fainter kN in this photometric region and, in order to match the observed

[1]Also the work presented in ref. (Villar et al. 2017b) employs a Gaussian likelihood, with the inclusion of an additional uncertainty parameter; while, in ref. (Coughlin et al. 2017), the authors proposed a likelihood distributed as a χ^2.

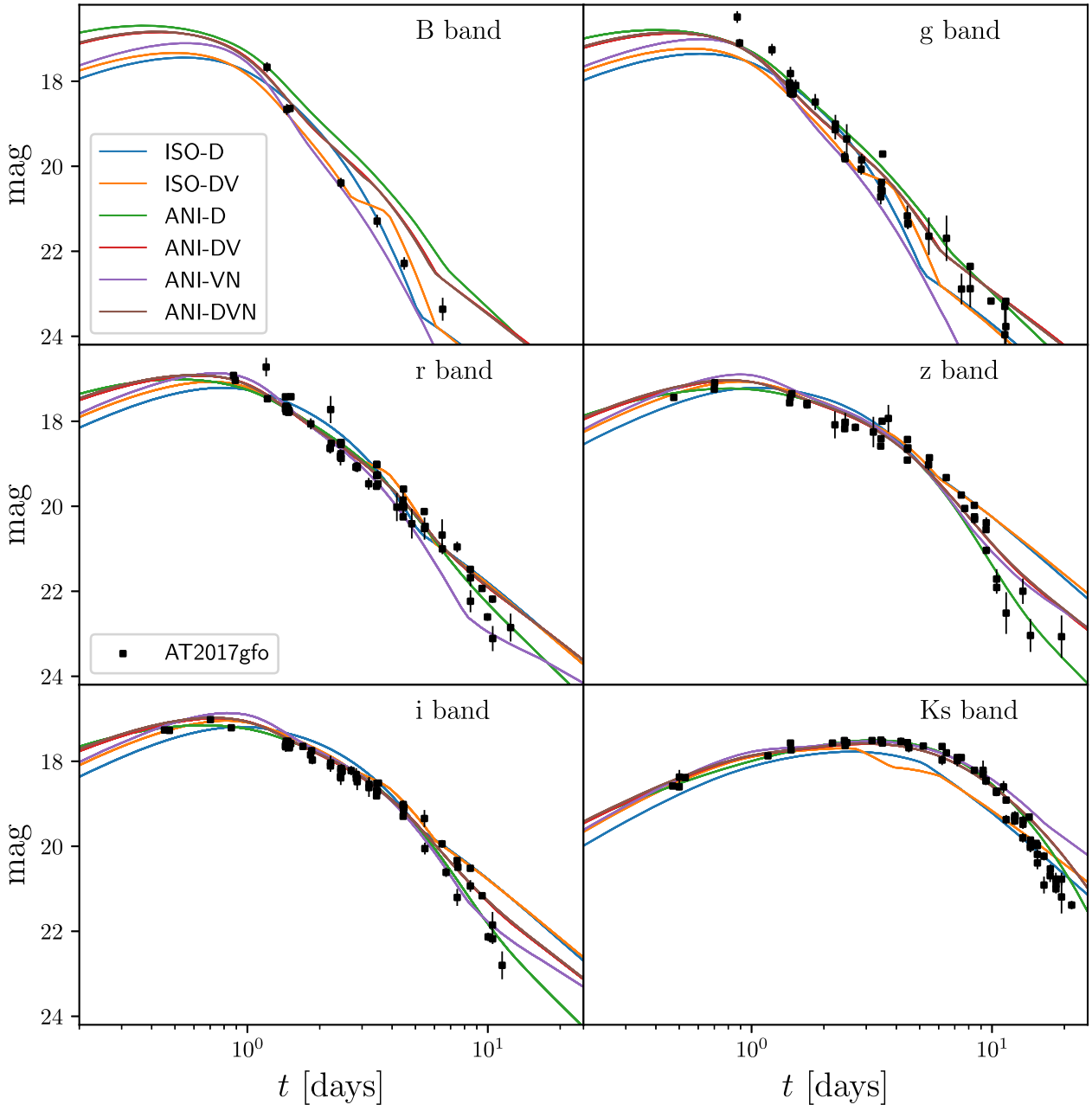

Figure 2. Apparent magnitudes computed using the maximum-likelihood parameter for each considered model; *ISO*-D in blue, *ISO*-DV in yellow, *ANI*-D in green, *ANI*-DV in red, *ANI*-VN in purple, and *ANI*-DVN in brown. The different panels refer to different photometric bands, respectively *B*, *g*, *r*, *z*, *i*, and *Ks*. The black squares are the observed data of AT2017gfo for the corresponding photometric band with the respective standard deviations.

data, the recovered heating rate are larger. Note that this bias concurs in the overestimation of the LC in the high-frequency bands (i.e. *U*, *B*, and *V*), where the number of measurements is lower with respect to the other employed bands.

4.3.1 ISO-*D*

We start considering the simplest employed model, the isotropic one-component model labelled as *ISO*-D. Fig. 4 shows the marginalized posterior distribution in the (m, $v_{\rm rms}$) plane. The velocity is constrained around $\sim 0.18\,c$ while the ejected mass lies around 8×10^{-3} $M_\odot$, both in agreement with the observational results recovered in ref. (Abbott et al. 2017d; Cowperthwaite et al. 2017; Villar et al. 2017b; Coughlin et al. 2018). Moreover, the opacity posterior peaks in proximity of $\kappa \sim 6$ cm^2 g^{-1}, consistently with ref. (Cowperthwaite et al. 2017).

Regarding the extrinsic parameters, the posterior for the inclination angle ι is coincident with the imposed prior, since the employed profiles do not depend on this coordinate. The model is not able to constrain the value of $T^{\rm Ni}_{\rm floor}$, which returns a posterior identical to the prior, while $T^{\rm LA}_{\rm floor}$ is recovered around 2500 K. The obtained flat posterior distribution for the $T^{\rm Ni}_{\rm floor}$ parameter highlights the unsuitability of this model in capturing the features of the observed data.

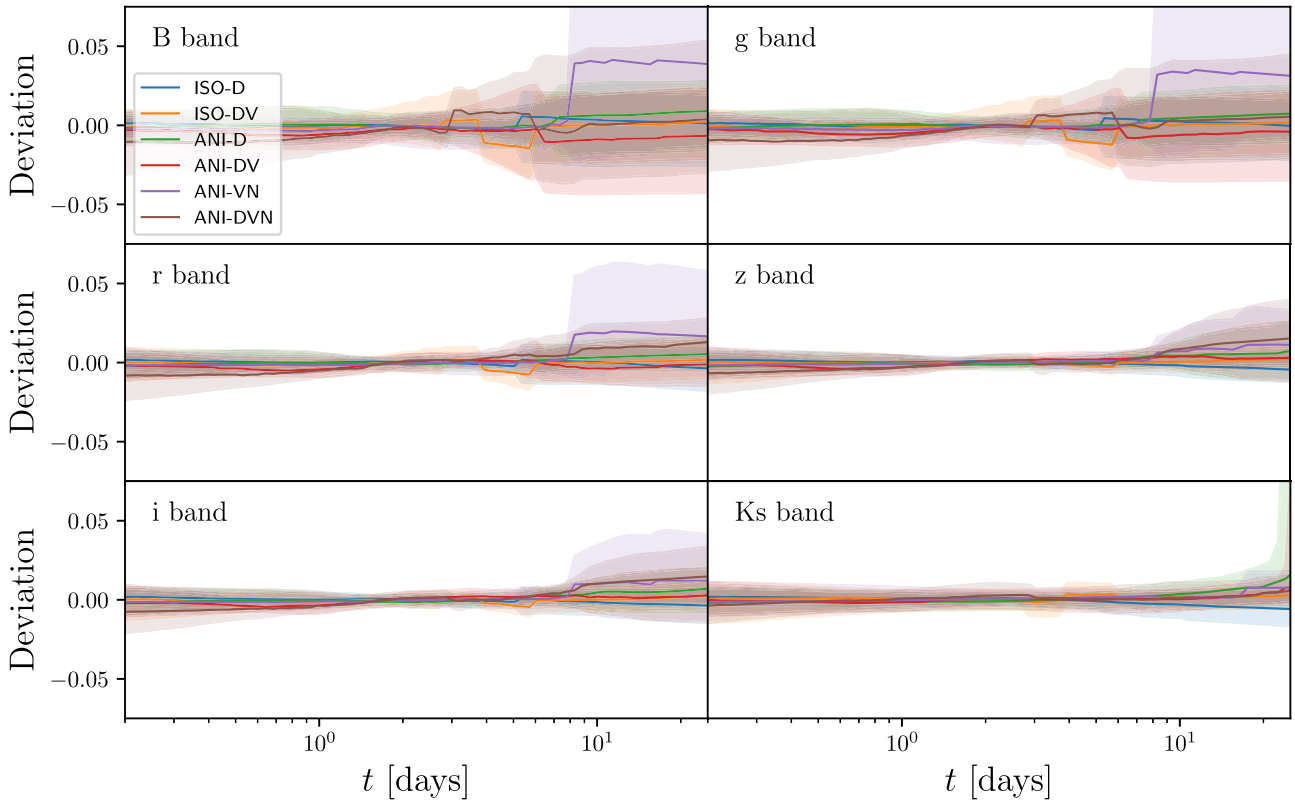

Figure 3. Deviations from the maximum-likelihood template of the LCs computed from the whole set of posterior samples. The solid lines represent the median values and the shadowed areas are the 90 per cent credible regions. Different colour refers to a different model; respectively, *ISO*-D in blue, *ISO*-DV in yellow, *ANI*-D in green, *ANI*-DV in red, *ANI*-VN in purple, and *ANI*-DVN in brown. The different panels show different photometric bands, respectively *B*, *g*, *r*, *z*, *i*, and *Ks*.

Table 2. Estimated log-evidences for the analysed kNe models. The reported uncertainties refers to the standard deviations estimated according to ref. (Skilling 2006).

Profile	Components	$\log p(d\|\text{Model})$
ISO	D	$-23\,510 \pm 1$
ISO	D+V	$-19\,719 \pm 1$
ANI	D	-9920 ± 1
ANI	N+V	$-11\,103 \pm 1$
ANI	D+V	-9556 ± 1
ANI	D+N+V	-9439 ± 1

4.3.2 ANI-*D*

For the anistropic single-component model *ANI*-D, the value of the ejected mass agrees with the one coming from the *ISO*-D case. However, in order to fit the data, *ANI*-D requires a larger velocity, $\sim 0.23\,c$, as shown in Fig. 4. The high-latitude opacity is constrained around the lower bound 0.1 $\text{cm}^2\,\text{g}^{-1}$ while the low-latitude contribution exceeds above 30 $\text{cm}^2\,\text{g}^{-1}$, which largely differs from the respective isotropic case, *ISO*-D. In practice, that is due to the lack of ejected mass that is balanced with a more opaque environment. Nevertheless, according to the estimated evidences, this model is preferred with respect to the isotropic case. The reason is clear from Fig. 2: the anisotropic model is able to characterize the late-times features of the data. The heating rate parameter ϵ_0 is largely biased towards larger values with respect to the results of ref. (Korobkin et al. 2012), in order to compensate the lack of ejected matter. Indeed, a larger heating factor ϵ_0 leads to brighter LCs, and this effect is capable to mimic an increase in the amount of ejected matter.

The posterior distribution for viewing angle ι peaks around 44 deg, inconsistently with the estimations coming from the GRB analysis (Abbott et al. 2017c; Savchenko et al. 2017; Ghirlanda et al. 2019). Moreover, unlike the *ISO*-D case, both temperature parameters $T_{\text{floor}}^{\text{Ni}}$ and $T_{\text{floor}}^{\text{LA}}$ are well constrained for the *ANI*-D analysis: these parameters affect mostly the late-times model, modifying the slope of the recovered LCs. Thus, these terms are responsible for the improvement in the fitted LCs.

4.3.3 ISO-*DV*

Fig. 5 shows the posterior distribution for some exemplary intrinsic ejecta parameters. For both components, the individual most-likely value for ejected mass parameter lies around $\sim 10^{-2}\ \text{M}_\odot$, in agreement with the measurement presented in ref. (Abbott et al. 2017d). This range of values is slightly overestimating the expectations coming from NR simulations for the dynamical component (Nedora et al. 2019; Perego et al. 2019; ; Bernuzzi et al. 2020; Endrizzi et al. 2020; Nedora et al. 2021). This could be explained by considering the effect of the spiral-wave wind (Nedora et al. 2019), which constitute a massive and fast ejecta on time-scales of 10–100 ms. The spiral-wave wind is not considered as components in our models because it would be highly degenerate with the dynamical ejecta. The recovered opacity parameters are roughly $4-5$ $\text{cm}^2\,\text{g}^{-1}$. The velocity of the dynamical component is greater than secular velocity, accordingly with the theoretical expectations. Comparing with other fitting

Table 3. Recovered values from the posterior distributions of the of the intrinsic ejecta parameters. The reported quantities are the means with the 90 per cent credible regions. The conventions $\gtrsim$, $\lesssim$ denote marginalized posterior distributions constrained respectively around the upper and the lower prior bounds. We remark that $\kappa_{\rm low}$ and $\kappa_{\rm high}$ refer respectively to the grey opacity parameters for low and high latitudes.

Model	Dynamical ejecta				Viscous ejecta			ν-driven wind		
	m $[10^{-2}{\rm M}_\odot]$	$v_{\rm rms}$ $[c]$	$\kappa_{\rm high}$	$\kappa_{\rm low}$ $[{\rm cm^2\,g^{-1}}]$	m $[10^{-2}{\rm M}_\odot]$	$v_{\rm rms}$ $[c]$	κ $[{\rm cm^2\,g^{-1}}]$	m $[10^{-2}{\rm M}_\odot]$	$v_{\rm rms}$ $[c]$	κ $[{\rm cm^2\,g^{-1}}]$
ISO-D	$0.787^{+0.016}_{-0.017}$	$0.1758^{+0.0007}_{-0.0008}$		$6.14^{+0.11}_{-0.10}$	–	–	– –	–	–	–
ISO-DV	$1.139^{+0.048}_{-0.044}$	$0.213^{+0.003}_{-0.003}$		$4.13^{+0.08}_{-0.09}$	$\lesssim$1	$\gtrsim$0.1	$4.99^{+0.12}_{-0.11}$	–	–	–
ANI-D	$0.807^{+0.022}_{-0.018}$	$0.236^{+0.001}_{-0.002}$	$\lesssim$0.1	$\gtrsim$30	–	–	– –	–	–	–
ANI-DV	$1.231^{+0.041}_{-0.048}$	$0.233^{+0.002}_{-0.002}$	$\lesssim$0.1	$12.3^{+0.6}_{-0.5}$	$\lesssim$1	$0.0276^{+0.0007}_{-0.0006}$	$2.23^{+0.05}_{-0.05}$	–	–	–
ANI-VN	–	–	–	–	$\lesssim$1	$0.0064^{+0.0001}_{-0.0001}$	$0.45^{+0.01}_{-0.01}$	$\gtrsim$0.75	$0.0998^{+0.0003}_{-0.0008}$	$1.002^{+0.006}_{-0.002}$
ANI-DVN	$1.378^{+0.063}_{-0.071}$	$0.233^{+0.002}_{-0.002}$	$\lesssim$0.1	$11.1^{+0.7}_{-0.6}$	$\lesssim$1	$0.0318^{+0.0008}_{-0.0008}$	$2.96^{+0.07}_{-0.09}$	$0.247^{+0.025}_{-0.061}$	$0.0502^{+0.0006}_{-0.0002}$	$2.29^{+0.14}_{-0.09}$

Table 4. Recovered values from the posterior distributions of the of the global intrinsic parameters and of the extrinsic parameters. The reported quantities are the means with the 90 per cent credible regions. The conventions $\gtrsim$, $\lesssim$ denote marginalized posterior distributions constrained respectively around the upper and the lower prior bounds.

Model	$T^{\rm Ni}_{\rm floor}$ (K)	$T^{\rm LA}_{\rm floor}$ (K)	ϵ_0 $[10^{18}{\rm erg\,g^{-1}\,s^{-1}}]$	ι (deg)	$D_{\rm L}$ (Mpc)
ISO-D	4335^{+3157}_{-3427}	2484^{+450}_{-410}	$66.5^{+1.5}_{-1.4}$	33^{+27}_{-25}	$\gtrsim$50
ISO-DV	6740^{+778}_{-612}	1126^{+243}_{-311}	$21.21^{+0.05}_{-0.05}$	34^{+24}_{-26}	$48.5^{+0.3}_{-0.4}$
ANI-D	5064^{+47}_{-50}	746^{+219}_{-223}	161^{+3}_{-5}	$43.9^{+0.5}_{-0.5}$	$\gtrsim$50
ANI-DV	5031^{+105}_{-99}	704^{+175}_{-180}	$38.7^{+0.9}_{-0.9}$	$43.9^{+0.5}_{-0.5}$	$\gtrsim$50
ANI-VN	3356^{+56}_{-35}	$\lesssim$500	$8.5^{+0.1}_{-0.1}$	52^{+1}_{-1}	$22.6^{+0.2}_{-0.2}$
ANI-DVN	5995^{+105}_{-118}	$\lesssim$500	$30.4^{+0.2}_{-0.1}$	57^{+1}_{-1}	$\gtrsim$50

Table 5. Estimated values of mass ratio q, reduced tidal parameter $\tilde{\Lambda}$, and NS radius $R_{1.4}$ measured from the analyses of AT2017gfo and GW170817. The $R_{1.4}$ are estimated using the relation proposed in ref. (De et al. 2018; Radice & Dai 2019) and employing the chirp mass posterior distribution coming from the GW analysis (Gamba et al. 2020a).

Data	q	$\tilde{\Lambda}$	$R_{1.4}$ (km)
AT2017gfo	$\lesssim$1.54	900^{+310}_{-780}	$13.46^{+0.93}_{-3.82}$
GW170817	$\lesssim$1.33	510^{+350}_{-320}	$12.33^{+1.22}_{-1.85}$
Combined	$\lesssim$1.27	460^{+210}_{-190}	$12.16^{+0.89}_{-1.11}$

models, the recovered ejected masses $m^{(\rm D)}$ result smaller with respect to the analogous analysis of ref. (Villar et al. 2017b), while the results roughly agree with the estimations coming from ref. (Coughlin et al. 2018). However, it is not possible to perform an apple-to-apple comparison between these results, due to the systematic differences in modelling between the semi-analytical model (used in this work) and the radiative-transport methods employed in ref. (Villar et al. 2017b; Coughlin et al. 2018).

The temperature parameters, $T^{\rm Ni}_{\rm floor}$ and $T^{\rm LA}_{\rm floor}$, are much more constrained comparing with the respective isotropic single component case *ISO*-D, and this is reflected in the improvement of fitting the different trends of the data in the high-frequency bands. The marginalized posterior distribution of the inclination angle is coincident with the prior, according with the isotropic description.

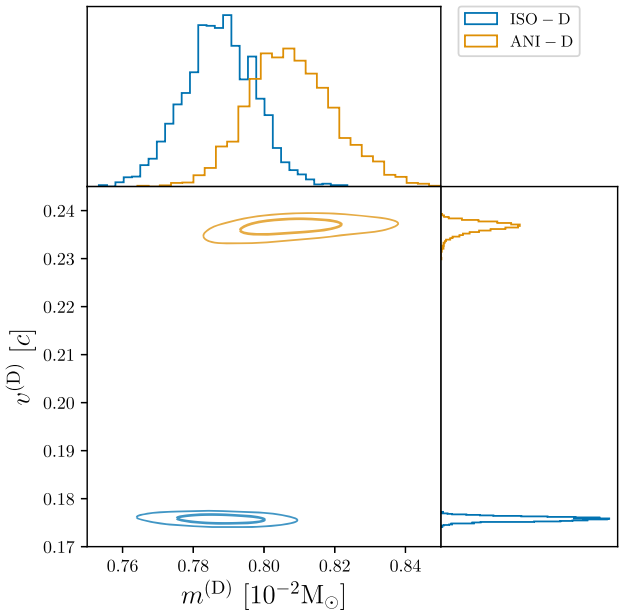

Figure 4. Marginalized posterior distribution of ejected mass m and velocity $v_{\rm rms}$ of dynamical component for the one-component studies, *ISO*-D and *ANI*-D. The anisotropic case requires larger velocities in order to fit the observed data.

Furthermore, the biases on the heating parameter ϵ_0 are reduced with respect to the *ISO*-D, since two-component case accounts for a larger amount of total ejected mass. Indeed, increasing the number of ejecta components other than the dynamical one, the overall kN becomes brighter since additional terms, becoming transparent at larger times, are included into the computation of the emitted flux. Then, ϵ_0 tends towards lower values in order to compensate this effect and fit the data. According with the estimated evidences, the isotropic two-components *ISO*-DV model is disfavoured with respect to the anisotropic single-component *ANI*-D. The main difficulty of *ISO*-DV is, again, to fit the data at late-times.

4.3.4 ANI-*DV*

The *ANI*-DV model is the second best-fitting model to AT2017gfo among the considered cases. Fig. 5 shows the posterior distribution for some exemplary intrinsic parameters of the dynamical and the viscous components. The ejected mass value lies around $\sim 10^{-2}$ ${\rm M}_\odot$, in agreement with previous estimates (Abbott et al. 2017d). On the

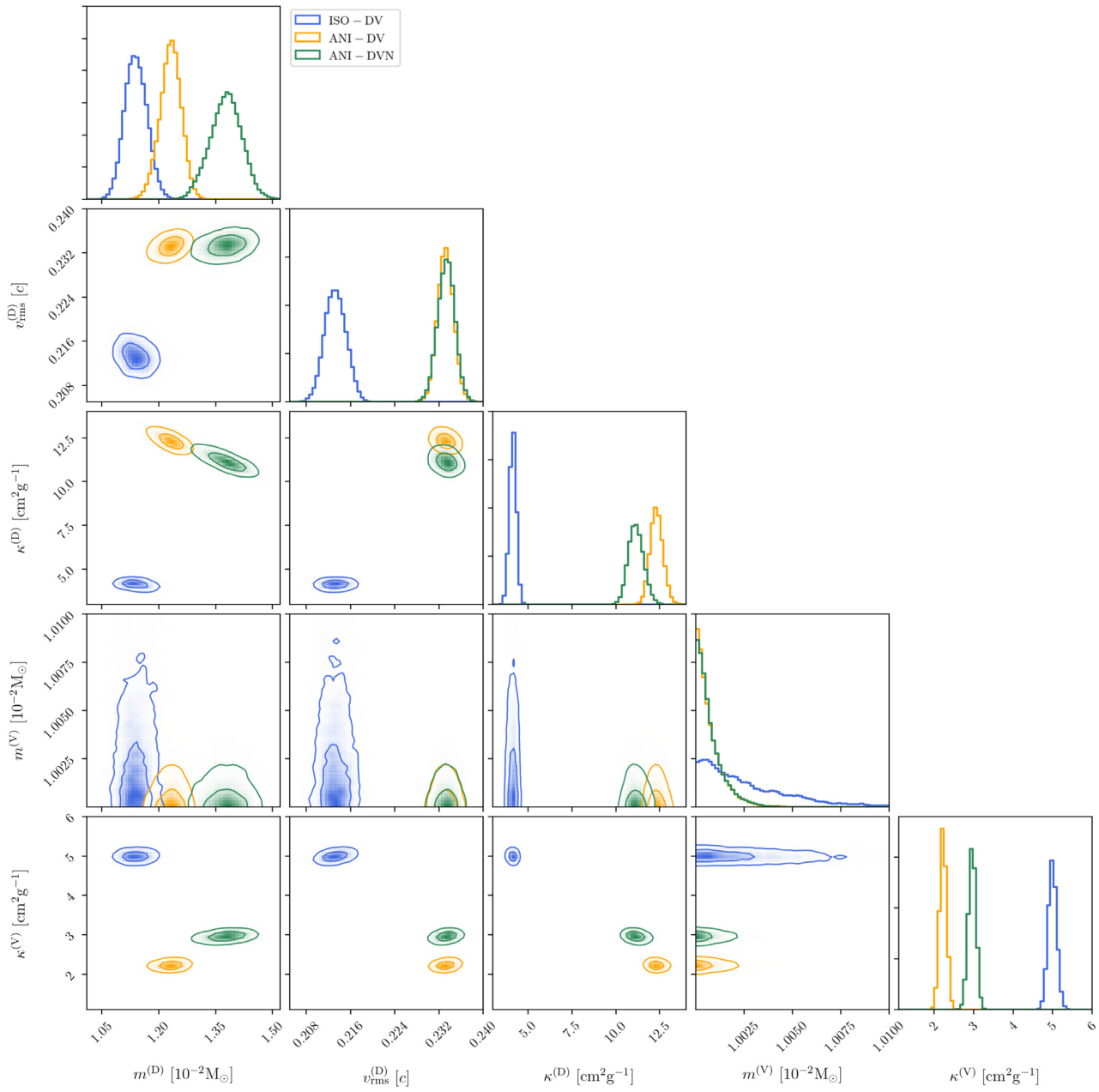

Figure 5. Marginalized posterior distribution for some exemplary ejecta intrinsic parameters extracted from the analysis of *ISO*-DV, *ANI*-DV, and *ANI*-DVN. The reported parameters are the ejected mass $m^{(D)}$, the velocity $v_{rms}{}^{(D)}$, and the low-latitude opacity $\kappa_{low}^{(D)}$ for the dynamical component, while for the viscous component, we report the ejected mass $m^{(V)}$ and the opacity $\kappa_{low}^{(V)}$. For *ISO*-DV, the low-latitude opacity of the dynamical component is replaced with the overall opacity $\kappa^{(D)}$, due to the different geometry.

other hand, the recovered mass slightly overestimates the results coming from targeted NR simulations (Nedora et al. 2019; Perego et al. 2019; Bernuzzi et al. 2020; Endrizzi et al. 2020; Nedora et al. 2021), similarly to *ISO*-DV (see Section 4.3.3). The velocity is well constrained around $\sim 0.23\,c$. The recovered low-latitude opacity corresponds roughly to 12 $cm^2\,g^{-1}$ and high-latitude opacity is constrained around the lower bound, 0.1 $cm^2\,g^{-1}$. This result can be explained by considering that the mass of the dynamical component slightly overshoots the NR expectations (Nedora et al. 2019; Perego et al. 2019; Bernuzzi et al. 2020; Endrizzi et al. 2020; Nedora et al. 2021; of a factor $\sim$1.25), and by noticing that the ejected mass correlates with the luminosity distance and the heating factor (that are generally biased). This combination generates the overestimation of the data in the NUV region. In order to improve the fitting to the observed data, the model tries to compensate this effect and the high-latitude opacity tends to move towards lower values.

Concerning the viscous component, its velocity results an order of magnitude smaller than the one of the dynamical ejecta, in agreement with the expectations. This enforce the hypothesis for which the viscous ejecta contributes mostly to the red kN. The posterior distribution of opacity parameter peaks around $\sim 5\,cm^2\,g^{-1}$, denoting a medium opaque environment.

Fig. 6 shows the posterior distribution for the extrinsic parameters. The temperatures T_{floor}^{Ni} and T_{floor}^{LA} are well constrained respectively

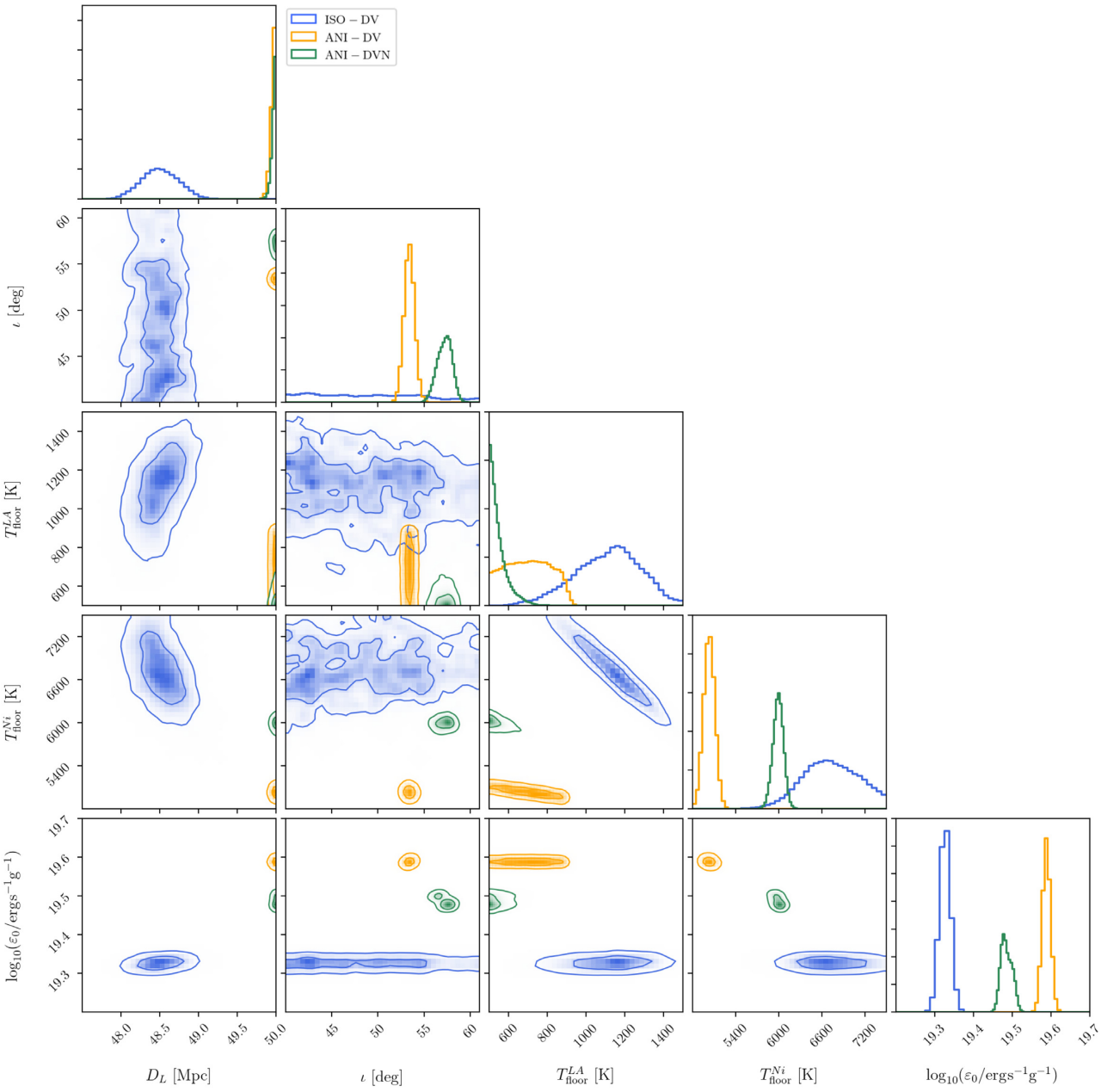

Figure 6. Marginalized posterior distribution for the global intrinsic parameters and the extrinsic parameters extracted from the analysis of *ISO*-DV, *ANI*-DV, and *ANI*-DVN. The reported parameters are luminosity distance $D_{\rm L}$, the viewing angle ι, the floor temperatures $T^{\rm LA}_{\rm floor}$ and $T^{\rm Ni}_{\rm floor}$ and the logarithm of the heating factor ϵ_0. For the *ISO*-DV case, the posterior distribution for the viewing angle ι coincides with prior due to the employed geometry.

around ∼5000 and ∼700 K. The agreement with ref. (Korobkin et al. 2012) on the estimation of the heating factor ϵ_0 increases with respect to the *ANI*-D case, due to the inclusion of an additional component, similarly to what is discussed in Section 4.3.3. The posterior for inclination angle results similar to the *ANI*-D case, according with the fact that the viscous component, as we have defined it, does not introduce further information on the inclination.

4.3.5 ANI-*VN*

According to Table 2, this *ANI*-VN is the least likely model among all anisotropic cases. As previously mentioned, the reason for this is clear from the LCs. The parameters of the viscous component are characterized by a slow velocity of $\sim 6\times10^{-3}\,c$ and a low opacity environment, $\kappa \sim 0.5$ cm^2 g^{-1}. On the other hand, the neutrino-driven wind mass is overestimated compared with aftermath computations presented in ref. (Perego et al. 2017a), in order to compensate the lack of overall ejected mass due to the absence of a dynamical component. Moreover, the neutrino-driven wind is characterized by a realistic velocity of $\sim 0.1\,c$, and by a low-opaque environment, $\kappa \sim 1$ cm^2 g^{-1}.

Regarding the extrinsic parameters, the *ANI*-VN model is the case that gives the best agreement with ref. (Korobkin et al. 2012) in terms of heating factor. The distance, instead, is recovered around ∼20 Mpc, underestimating the GW distance (Abbott et al. 2017a). This result could be explained by the lower amount of total ejected

mass and by the lower heating rate compared with the other cases (see Table 3): this lack generates fainter kN that biases the source to appears closer to the observer in order to fit the data. The $T_{\rm floor}^{\rm Ni}$ parameter takes lower values (∼3300 K) comparing with the *ANI*-DV case (∼5000 K), since the model has to fit the data employing a polar geometry (N) instead of an equatorial ejecta (D). The viewing angle is biased towards larger values, roughly ∼50 deg, inconsistent with GRB expectations (Abbott et al. 2017c; Savchenko et al. 2017).

4.3.6 ANI-*DVN*

This is the model that gives the largest evidence, within the provided prior bounds. Regarding the dynamical and viscous ejecta components, the general features are similar to the one of the *ANI*-DV case. The dynamical ejected mass is slightly overestimated comparing with NR simulations (Nedora et al. 2019; Perego et al. 2019; Bernuzzi et al. 2020; Endrizzi et al. 2020; Nedora et al. 2021) of a factor ∼2. The dynamical component is described by a low-opacity environment for high latitudes ($\kappa_{\rm high} \sim 0.1$ cm^2 g^{-1}) and high opacity for low latitudes ($\kappa_{\rm low} \sim 11$ cm^2 g^{-1}), in agreement with NR simulations (Nedora et al. 2019; Perego et al. 2019; Bernuzzi et al. 2020; Endrizzi et al. 2020; Nedora et al. 2021). These results approximately agree also with other observational estimations (e.g. Cowperthwaite et al. 2017; Villar et al. 2017b; Abbott et al. 2017d; Coughlin et al. 2018) Furthermore, the 'D' component results into the fasted ejected shell, validating the interpretation that this contribution is generated at dynamic timescales. On the other hand, the viscous ejecta is characterized by an average opacity ∼3 cm^2 g^{-1} and by low velocity $\sim 3\times10^{-3}\,c$, an order of magnitude smaller then the one of the dynamical ejecta. These results agree with the studies presented in ref. (Radice et al. 2018c) and they contribute to the LCs in the optical band.

Regarding the neutrino-driven wind, the posterior distribution for its ejected mass $m^{(\rm N)}$ shows a bimodality and this degeneracy correlates with the heating rate parameter ϵ_0. This behaviour can be seen in Fig. (7), which shows the marginalized posterior distribution for ϵ_0 and for the total ejected mass $M_{\rm ej}$, defined as

$$M_{\rm ej} = \sum_{k={\rm D,N,V}} m^{(k)}, \tag{14}$$

where the index k runs over all the involved components. The marginalized posterior distribution for $m^{(\rm N)}$ has its dominat peak in proximity of 2.5×10^{-3} M$_\odot$, while the secondary mode is located slightly below 2×10^{-3} M$_\odot$. Despite the bimodality, the recovered values of $m^{(\rm N)}$ are smaller compared with the same parameter extracted from the *ANI*-VN analysis. These results are largely consistent with aftermath computations (Perego et al. 2014) and with theoretical expectations (Perego et al. 2017a), as it is for the recovered velocity and opacity parameters.

Furthermore, also for the *ANI*-DVN case, the viewing angle is biased towards larger values, roughly ∼60 deg. The same trend is shown by the anisotropic three-component model employed in ref. (Villar et al. 2017b). The posterior distribution for the $T_{\rm floor}^{\rm Ni}$ parameter peaks around ∼6000 K, while, the temperature $T_{\rm floor}^{\rm LA}$ is constrained around the lower bound, 500 K.

5 EOS INFERENCE

The combination of gravitational and EM signals coming from the same compact binary merger allows the possibility to constrain more tightly the intrinsic properties of the system and the nuclear EOS, in the context of both BNS (e.g. Radice et al. 2018b; Radice & Dai 2019) and black hole-NS mergers (e.g. Barbieri et al. 2019). In this section, we apply the information coming from NR-fitting formulae (Nedora et al. 2021, 2020) to the posterior distribution of the preferred kN model (*ANI*-DVN), in order to infer the mass ratio and the reduced tidal parameter of the BNS source. Subsequently, we combine the kN and GW results to derive constraints on the radius $R_{1.4}$ of an irrotational NS of 1.4 M$_\odot$.

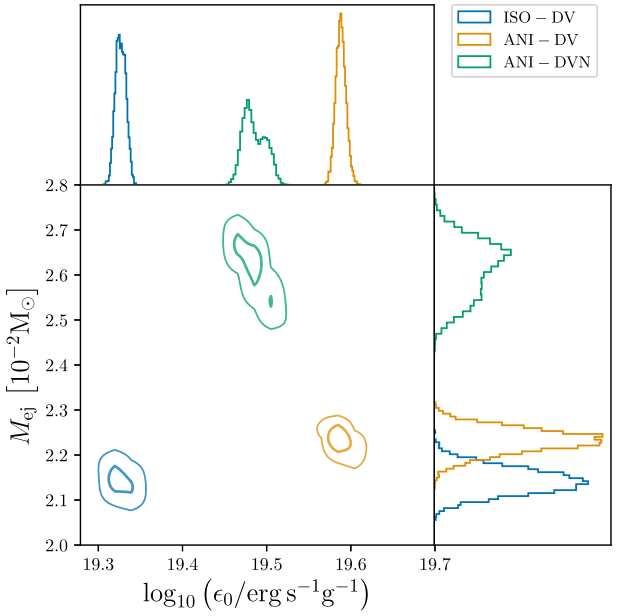

Figure 7. Marginalized posterior distribution of heating parameter ϵ_0 and total ejected mass $M_{\rm ej}$ for three selected cases: *ISO*-DV (blue), *ANI*-DV (yellow), and *ANI*-DVN (green). The heating parameter ϵ_0 is plotted using the logarithm to base 10 in order to evince the recovered orders of magnitude. The total mass $M_{\rm ej}$ is computed extending the sum to all the involved components.

5.1 Mass ratio and reduced tidal parameter

A BNS is characterized by the masses of the two objects, m_1 and m_2, and by the tidal quadrupolar polarizability coefficients,

$$\Lambda_i = \frac{2}{3} k_{2,i} C_i^{-5}, \tag{15}$$

where $k_{2,i}$ is the quadrupolar Love number, $C_i = Gm_i/(R_i c^2)$ the compactness of star, G the gravitational constant, R_i the radius of the star, and $i = 1, 2$. Furthermore, we introduce the mass ratio $q = m_1/m_2 \geq 1$ and the reduced tidal parameter $\tilde{\Lambda}$ as:

$$\tilde{\Lambda} = \frac{16}{13} \frac{(q+12)q^4\Lambda_1 + (1+12q)\Lambda_2}{(1+q)^5}. \tag{16}$$

The NR fits presented in ref. (Nedora et al. 2020) use simulations targeted to GW170817 (Nedora et al. 2019; Perego et al. 2019; Bernuzzi et al. 2020; Endrizzi et al. 2020; Nedora et al. 2021) and give the mass $m^{(\rm D)}$ and velocity $v_{\rm rms}{}^{(\rm D)}$ of the dynamical ejecta as functions of the BNS parameters (q, $\tilde{\Lambda}$). In order to recover the posterior distribution of the latter, we adopt a resampling method, similar to the procedure presented in ref. (Coughlin et al. 2017, 2018): a sample (q, $\tilde{\Lambda}$) is extracted from the prior distribution,[2] exploiting

[2]The prior distribution is taken uniformly distributed in the tidal parameters $\tilde{\Lambda}$; while, regarding the mass ratio q, we employ a prior distribution uniform in the mass components, which corresponds to a probability density proportional

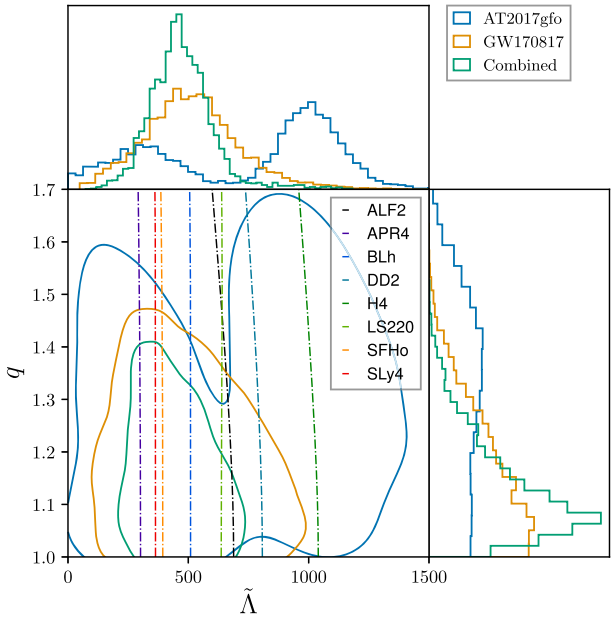

Figure 8. Posterior distribution in the $(\tilde{\Lambda}, q)$ plane. The blue solid lines refer to the resampled values extracted from the kN analysis (*ANI*-DVN). The orange solid lines refer to the GW results, where the samples have been reweighted over a flat prior in $\tilde{\Lambda}$. The green solid lines are the combined inference. The contours represent the 90 per cent credible regions The plot shows the expectations of some representative EOS.

the ranges $q \in [1, 2]$ and $\tilde{\Lambda} \in [0, 5000]$. Subsequently, the tuple $(q, \tilde{\Lambda})$ is mapped into the dynamical ejecta parameters $(m^{(\mathrm{D})}, v_{\mathrm{rms}}{}^{(\mathrm{D})})$ using the NR formulae presented in ref. (Nedora et al. 2020). The likelihood is estimated in the dynamical ejecta parameter space using a kernel density estimation of the marginalized posterior distribution recovered from the preferred model (*ANI*-DVN). Furthermore, since NR relations have non-negligible uncertainties, we introduce calibration parameters α_1, α_2, such that

$$\log_{10} m^{(\mathrm{D})} = (1+\alpha_1)\cdot \log_{10} m^{(\mathrm{D})}_{\mathrm{fit}}(q, \tilde{\Lambda}),$$
$$v_{\mathrm{rms}}{}^{(\mathrm{D})} = (1+\alpha_2)\cdot v_{\mathrm{rms\,fit}}{}^{(\mathrm{D})}(q, \tilde{\Lambda}). \quad (17)$$

The calibrations parameters $\alpha_{1,2}$ are sampled along the other parameters using a normally distributed prior with vanishing means and standard deviations prescribed by the relative uncertainties of NR fits equal to 0.2 for both. The resampled posterior distribution is marginalized over the calibration parameters. The BNS parameter space is explored using a Metropolis–Hasting technique. Note that a correct characterization of the fit uncertainty is crucial, since this contribution is the largest source of error in the inference of $(q, \tilde{\Lambda})$.

The posterior distribution in the $(q, \tilde{\Lambda})$ plane as obtained from the dynamical ejecta properties fitted to AT2017gfo data is shown in Fig. 8 and Table 5 shows the median values. The measurement of the tidal parameter leads to $\tilde{\Lambda} = 900^{+310}_{-780}$, with a bimodality in the marginalized posterior distribution, due to the quadratic nature of the employed NR formulae, with modes $\tilde{\Lambda} \sim 370$ and $\tilde{\Lambda} \sim 1000$. The mass ratio is constrained to be lower than 1.54 at the 90 per cent confidence level. The uncertainties of these estimations are larger than those of the GW analyses (Abbott et al. 2017a, 2019a; Gamba et al. 2020a) and the principal source of error is the uncertainty of the NR fit formulae.

Fig. 8 and Table 5 show also the results coming from the GW170817 analysis extracted from ref. (Gamba et al. 2020a). For this analysis, the data correspond to the LIGO-Virgo strains (Abbott et al. 2017a, 2019a,b) centred around GPS time 1187008882 with sampling rate of 4096 Hz and duration of 128 s. The parameter estimation has been performed with the nested sampling provided by the PBILBY pipeline (Ashton et al. 2019; Smith et al. 2020) employing the effective-one-body waveform approximant TEOBRESUMSPA (Nagar et al. 2018; Gamba et al. 2020a) and analysing the frequency range from 23 to 1024 Hz.[3] Furthermore, the GW posterior samples have been reweighted with a rejection sampling to the prior distributions employed in the kN study, in order to use the same prior information for both analyzes.[4]

Under the assumption that GW170817 and AT2017gfo are generated by the same physical event, the $(q, \tilde{\Lambda})$ posterior distributions coming from the two independent analyses can be combined, in order to constrain the estimation of the inferred quantities. The joint probability distribution is computed as the product of the single terms,

$$p(q, \tilde{\Lambda}|d_{\mathrm{kn}}, d_{\mathrm{gw}}) = p(q, \tilde{\Lambda}|d_{\mathrm{kn}}) \cdot p(q, \tilde{\Lambda}|d_{\mathrm{gw}}), \quad (18)$$

and the samples are extracted with a rejection sampling. The combined inference, shown in Fig. 8, leads to a constraint on the mass ratio of $\lesssim 1.27$ and on the tidal parameter $\tilde{\Lambda} = 460^{+210}_{-190}$, at the 90 per cent confidence levels. Imposing these bounds, stiff nuclear EOS, such as DD2, are disfavoured.

5.2 Neutron-star radius

Using the universal relation presented in ref. (De et al. 2018; Radice & Dai 2019), it is possible to impose a constraint on the radius $R_{1.4}$ of a NS of 1.4 $\mathrm{M}_\odot$. We employ the marginalized posterior distribution for the (source-frame) chirp mass $\mathcal{M} = (m_1 m_2)^{3/5}/(m_1+m_2)^{1/5}$ coming from the GW170817 measurement (Gamba et al. 2020a) and the posterior on the tidal parameter $\tilde{\Lambda}$ obtained with the joint analyses AT2017gfo+GW170817. We adopt a resampling technique to account for the uncertainties in the universal relation, introducing a Gaussian calibration coefficient with variance prescribed by ref. (De et al. 2018; Radice & Dai 2019). We estimate $R_{1.4} = 12.16^{+0.89}_{-1.11}$ km. The presented measurement agrees with the results coming from literature (Annala et al. 2018; De et al. 2018; Abbott et al. 2018b; Coughlin et al. 2019; Radice & Dai 2019; Capano et al. 2020; Dietrich et al. 2020; Essick et al. 2020; Raaijmakers et al. 2020) and its overall error at 1σ level corresponds roughly to 500 m.

In Fig. 9, the $R_{1.4}$ estimation is compared with the mass-radius curves from a sample of nuclear EOS. Our bounds impose observational constraints on the nuclear EOS, excluding both very stiff EOS, such as DD2, BHB$\Lambda\phi$, and MS1b, and very soft equations, such as 2B.

to $[(1+q)/q^3]^{2/5}$, analogously to GW analyses (Abbott et al. 2017a; Gamba, Bernuzzi & Nagar 2020a).

[3]This choice minimizes waveform systematics (Gamba et al. 2020b). On the other hand, it implies slightly larger statistical uncertainties on the reduced tidal parameters. Hence, our results are more conservative than previous multimessenger analyses in the treatment of uncertainties of GW data.

[4]The prior distribution for the tidal parameters employed in ref. (Gamba et al. 2020a) is uniform in the tidal components $\Lambda_{1,2}$; while, in our study, we used a uniform prior in $\tilde{\Lambda}$.

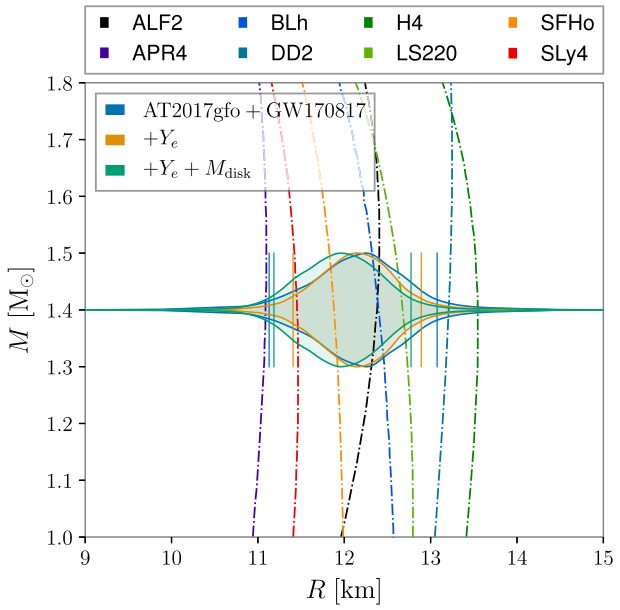

Figure 9. Posterior distribution of the radius $R_{1.4}$ estimated with the joined inference of AT2017gfo and GW170817 plotted on top of the mass–radius relations coming from a sample of nuclear EOS (dashed lines). The blue solid line is computed using the mass and velocity information of the dynamical component, the orange solid curve takes into account also the contribution of the electron fraction, and the green solid line is the result with the additional inclusion of the disc mass information.

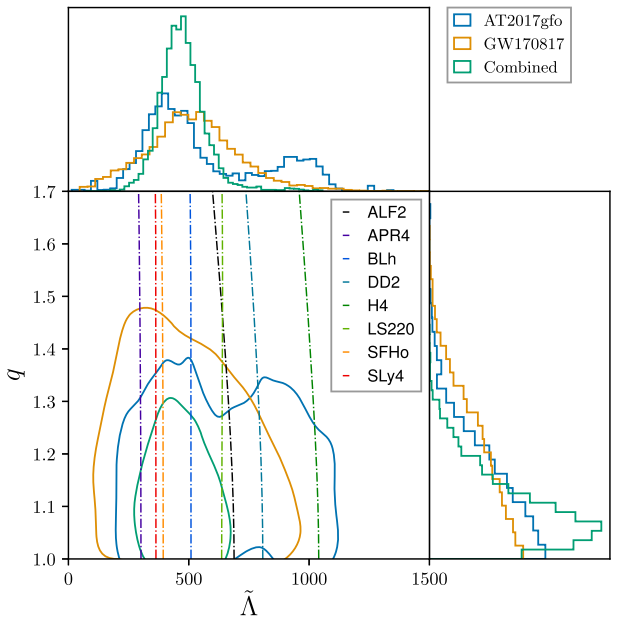

Figure 10. Posterior distribution in the $(\tilde{\Lambda}, q)$ plane, analogously to Fig. 8, including the contribution of the electron fraction Y_e.

5.3 Incorporating information from electron fraction and disc mass

We conduct two further analyses, in order to show that the contribution of additional NR information can improve the previous estimation. In the first case, we take into account the contribution of the electron fraction; while, in the second, we include the information on the disc mass. These studies are discussed in the following paragraphs and they are intended to represent proofs-of-principle analyses, since they involve extra assumptions on the ejecta parameters and their relation with the EOS properties. A more accurate mapping between these quantities will be discussed in a further study.

5.3.1 Electron fraction

From NR simulations, it is possible to estimate the average electron fraction, Y_e, of the dynamical ejecta (Nedora et al. 2020, 2021). This quantity is the ratio of the net number of electrons to the numer of baryons and it is strictly related with the opacity of the shell (Lippuner & Roberts 2015; Miller et al. 2019; Perego et al. 2019), since it mostly determines the nucleosynthesis yields in low entropy, neutron-rich matter. We compute the average opacity $\bar{\kappa}$ of a shell as the integral of the opacity over the polar angle weighted on the mass distribution,

$$\bar{\kappa} = \frac{1}{m}\int_0^\pi \varrho(\theta)\,\kappa(\theta)\,\sin\theta\,\mathrm{d}\theta. \tag{19}$$

Imposing the assumptions on the profiles of the dynamical ejecta, we get

$$\bar{\kappa}^{(\mathrm{D})} = \left(\frac{1}{2}+\frac{1}{\pi}\right)\kappa_{\rm low}^{(\mathrm{D})} + \left(\frac{1}{2}-\frac{1}{\pi}\right)\kappa_{\rm high}^{(\mathrm{D})}. \tag{20}$$

Thanks to this definition, it is possible to map the opacity $\bar{\kappa}$ into the electron fraction Y_e, using the relation presented in ref. (Tanaka et al. 2020). Subsequently, the Y_e can be related with the BNS parameters $(q, \tilde{\Lambda})$, using NR fit formulae (Nedora et al. 2020). We introduce an additional calibration parameter α_3, such that

$$Y_e = (1+\alpha_3)\cdot {Y_e}^{\rm fit}(q, \tilde{\Lambda}), \tag{21}$$

with a Gaussian prior with mean zero and standard deviation of 0.2. In this way, it is possible to take into account also the contribution of the opacity posterior distribution, introducing additional constraints on the inference of the NS matter.

The results are shown in Fig. 10. This further contribution has a strong effect on the mass ratio, constraining it to be $\lesssim$1.26. This effect is motivated by the fact that high-mass-ratio BNS mergers are expected to have $Y_e \lesssim 0.1$ (Bernuzzi et al. 2020; Nedora et al. 2021). The recovered electron fraction correspond to $Y_e = 0.20^{+0.03}_{-0.05}$. Regarding the tidal parameter, the Y_e information affects the importance of the modes, improving the agreement with GW estimations (Abbott et al. 2017a, 2019a; Gamba et al. 2020a), and it reduces the support of the posterior distribution, leading to an estimation of $\tilde{\Lambda} = 480^{+550}_{-220}$. Combining kN and GW posterior distribution, we estimate an upper bound on the mass ratio of 1.20 and a tidal parameter $\tilde{\Lambda} = 465^{+175}_{-130}$, which corresponds to $R_{1.4} = 12.14^{+0.75}_{-0.73}$ km, at the 90 per cent confidence level.

5.3.2 Disc mass

The employed kN model contains information also on the baryonic wind ejecta. These components are expected to be generated by the disc that surrounds the remnant (Metzger & Fernández 2014; Just et al. 2015; Kasen, Fernández & Metzger 2015), if present. The disc mass can be estimated from NR simulations as function of the BNS parameters $(q, \tilde{\Lambda})$, albeit with large uncertainties (Radice et al. 2018b, d; Nedora et al. 2020). We map a fraction ξ of the disc mass

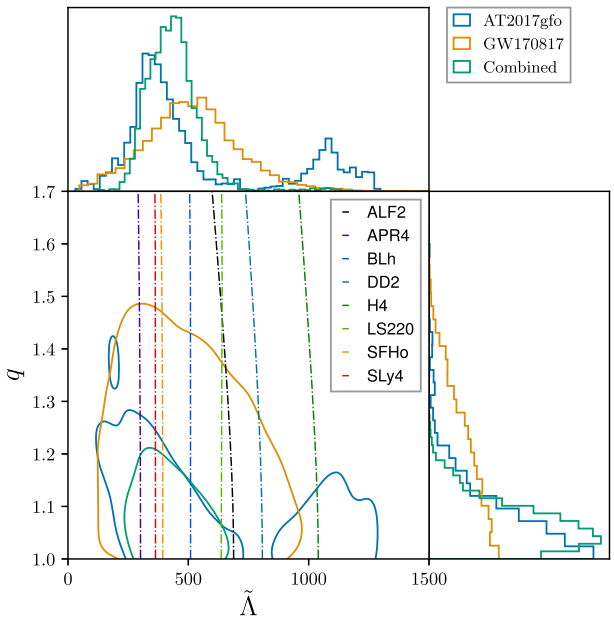

Figure 11. Posterior distribution in the $(\tilde{\Lambda}, q)$ plane, analogously to Fig. 8, including the contributions of electron fraction Y_e and disc mass $M_{\rm disc}$.

$M_{\rm disc}$ into the mass of the baryonic wind components,

$$m^{(\rm V)} + m^{(\rm N)} = \xi \cdot M_{\rm disc}. \tag{22}$$

The mass fraction ξ is sampled along the other parameters with a uniform prior in the range [0.1, 0.5]. We include the disc mass information together with the electron fraction contribution, previously discussed.

The results are shown in Fig. 11. The disc mass contribution slightly reinforces the constraint on the mass ratio posterior, giving the 90 per cent confidence level for $q = 1.18$. The distribution of the tidal parameter $\tilde{\Lambda}$ is sparser with respect to the case discussed in Section 5.3.1, due to the correlations induced by the $M_{\rm disc}$ formula. The electron fraction results $Y_e = 0.20^{+0.04}_{-0.08}$; while, the mass fraction corresponds to $\xi = 0.14^{+0.27}_{-0.04}$. The joined inference with the GW posterior leads to a mass ratio $\lesssim 1.13$ and a tidal parameter of $\tilde{\Lambda} = 430^{+180}_{-140}$, at the 90 per cent confidence. This result can be translated in a radius of $R_{1.4} = 11.99^{+0.82}_{-0.85}$ km.

6 CONCLUSION

In this paper, we have performed informative model selection on kN observations within a Bayesian framework applied to the case of AT2017gfo, the kN associated with the BNS merger GW170817. We have then combined the posteriors obtained from the kN observation with the ones extracted from the GW signal and with NR-based fitting formulae on the ejecta and remnant properties to set tight constraints on the NS radius and EOS.

From the analysis of AT2017gfo, the anisotropic description of the ejecta components is strongly preferred with respect to isotropic profiles, with a logarithmic Bayes' factor of the order of $\sim 10^4$. Moreover, the favoured model is the three-component kN constituted by a fast dynamical ejecta (comprising both a red-equatorial and a blue-polar portion), a slow isotropic shell and a polar wind. The best-fitting model inference overestimates the dynamical-ejected mass with respect to theoretical NR expectations by about a factor of two (Nedora et al. 2019; Perego et al. 2019; Bernuzzi et al. 2020; Endrizzi et al. 2020; Nedora et al. 2021). These biases can be explained by considering the effect of the spiral-wave wind (Nedora et al. 2019) and taking into account the correlations between the extrinsic parameters. The recovered velocity of the dynamical component agrees with NR simulations (Nedora et al. 2019; Perego et al. 2019; Bernuzzi et al. 2020; Endrizzi et al. 2020; Nedora et al. 2021), reinforcing the interpretation of this ejecta component. The intrinsic properties of the dynamical ejecta component are in agreement with previous results (Villar et al. 2017b; Coughlin et al. 2019). Regarding the secular winds, the neutrino-driven mass and velocity are compatible with the calculations of ref. (Perego et al. 2014, 2017a). The viscous component is the slowest contribution and is broadly compatible with the estimates of ref. (Radice et al. 2018c) that are inferred from NR and other disc simulations. The viewing angle resulting from the preferred kN model is larger than the one deduced from independent analysis (Abbott et al. 2017c; Savchenko et al. 2017; Ghirlanda et al. 2019), and also different from the one obtained by previous application of the same kN model (Perego et al. 2017a). In the latter case, and differently from the present analysis, the profile of the viscous ejecta was assumed to be mostly distributed across the equatorial angle. This discrepancy confirms the non-trivial dependence of the LCs from the ejecta geometry and distributions.

Under a modelling perspective, current kN description contains large theoretical uncertainties, such as thermalization effects, heating rates, and energy-dependent photon opacities e.g. (Zhu et al. 2021). These effects propagate into systematic biases in the global parameters of the model, as shown in the posterior distributions for luminosity distance $D_{\rm L}$ and heating rate parameter ϵ_0. Hence, the development and the improvements of kN templates is an urgent task in order to conduct reliable and robust analyses in the future.

We use the preferred kN model to constrain the properties of the progenitor BNS and the EOS of dense, cold matter. Combining the kN measurement with the information coming from NR simulations, the ejecta properties are mapped in terms of mass ratio and reduced tidal deformability of the binary progenitor. Subsequently, this information is combined with the measurements of the GW data. The joint kN+GW analysis constrains the reduced tidal parameter to $\tilde{\Lambda} = 460^{+210}_{-190}$ and the mass ratio of the BNS system to be lower than 1.27 at the 90 per cent credible level. Furthermore, the joint analysis predicts a radius for a NS of 1.4 $M_\odot$ approximately of $R_{1.4} \approx 12.2$ km with an uncertainty of $\sim$500 m at 1σ level. The $R_{1.4}$ estimation can be further improved including additional physical information extracted from the kN model in the inferred model, such as the electron fraction of the dynamical ejecta and the mass of the disc around the merger remnant. Fig. 12 summarizes ours and the current estimations of $R_{1.4}$ extracted from literature (Annala et al. 2018; De et al. 2018; Radice et al. 2018b; Abbott et al. 2018b; Coughlin et al. 2019; Radice & Dai 2019; Capano et al. 2020; Dietrich et al. 2020; Essick et al. 2020; Jiang et al. 2020; Raaijmakers et al. 2020).

In addition to the kN modelling uncertainties discussed above, another source of error of our estimates is the accuracy of the NR formulae. The relations employed here used exclusively targeted data and simulations with state-of-art treatment of microphysical EOS and neutrino treatment (Nedora et al. 2019; Perego et al. 2019; Bernuzzi et al. 2020; Endrizzi et al. 2020; Nedora et al. 2021). However, the simulation sample is limited to about hundrends of simulations, with fitting errors that could be reduced by considering data at even higher grid resolutions (Nedora et al. 2020). For example, assuming all the fit formulae to be exact (i.e. removing all calibration terms), it will be possible to infer the $\tilde{\Lambda}$ parameter

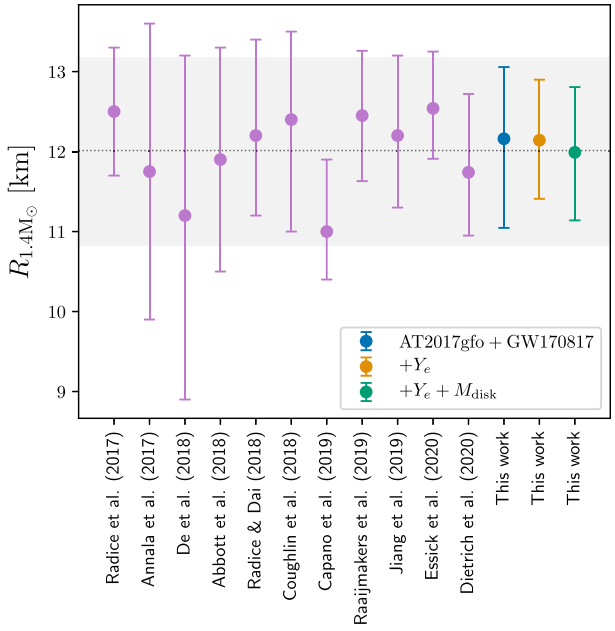

Figure 12. Summary plot of the current estimations of $R_{1.4}$. The reported values are the means and the 90 per cent credible regions extracted from refs. (Annala et al. 2018; De et al. 2018; Abbott et al. 2018b; Radice et al. 2018b; Coughlin et al. 2019; Radice & Dai 2019; Capano et al. 2020; Dietrich et al. 2020; Essick et al. 2020; Jiang et al. 2020; Raaijmakers et al. 2020). The dashed line and the shadowed area are respectively the average over all the current estimations and the respective 90 per cent credible region, corresponding to $R_{1.4} = 12.0^{+1.2}_{-1.2}$ km.

from a kN observation with an accuracy of the order of 10, which corresponds to a constraint on the radius $R_{1.4}$ of roughly 100 m.

ACKNOWLEDGEMENTS

MB and SB acknowledge support by the European Union's H2020 under ERC Starting Grant, grant agreement no. BinGraSp-714626. DR acknowledges support from the U.S. Department of Energy, Office of Science, Division of Nuclear Physics under Award Number(s) DE-SC0021177 and from the National Science Foundation under grant no. PHY-2011725. The computational experiments were performed on the ARA cluster at Friedrich Schiller University Jena supported in part by DFG grants INST 275/334-1 FUGG and INST 275/363-1 FUGG, and ERC Starting Grant, grant agreement no. BinGraSp-714626. Data postprocessing was performed on the Virgo "Tullio" server at Torino supported by INFN. This research has made use of data, software, and/or web tools obtained from the Gravitational Wave Open Science Center (`https://www.gw-openscience.org`), a service of LIGO Laboratory, the LIGO Scientific Collaboration, and the Virgo Collaboration. LIGO Laboratory and Advanced LIGO are funded by the United States National Science Foundation (NSF) as well as the Science and Technology Facilities Council (STFC) of the United Kingdom, the Max-Planck-Society (MPS), and the State of Niedersachsen/Germany for support of the construction of Advanced LIGO and construction and operation of the GEO600 detector. Additional support for Advanced LIGO was provided by the Australian Research Council. Virgo is funded, through the European Gravitational Observatory (EGO), by the French Centre National de Recherche Scientifique (CNRS), the Italian Istituto Nazionale della Fisica Nucleare (INFN), and the Dutch Nikhef, with contributions by institutions from Belgium, Germany, Greece, Hungary, Ireland, Japan, Monaco, Poland, Portugal, and Spain.

DATA AVAILABILITY

The observational data underlying this article were provided by (Villar et al. 2017b) under license. The posterior samples presented in this work will be shared on request to the corresponding author.

REFERENCES

Aasi J. et al., 2015, Class. Quantm. Grav., 32, 074001
Abbott B. P. et al., 2017a, Phys. Rev. Lett., 119, 161101
Abbott B. P. et al., 2017b, ApJ, 848, L12
Abbott B. P. et al., 2017c, ApJ, 848, L13
Abbott B. P. et al., 2017d, ApJ, 850, L39
Abbott B. P. et al., 2018a, Living Rev. Rel., 21, 3
Abbott B. P. et al., 2018b, Phys. Rev. Lett., 121, 161101
Abbott B. P. et al., 2019a, Phys. Rev., X9, 011001
Abbott B. P. et al., 2019b, Phys. Rev., X9, 031040
Acernese F. et al., 2015, Class. Quantum Grav., 32, 024001
Agathos M., Zappa F., Bernuzzi S., Perego A., Breschi M., Radice D., 2020, Phys. Rev., D101, 044006
Ajello M. et al., 2016, ApJ, 819, 44
Annala E., Gorda T., Kurkela A., Vuorinen A., 2018, Phys. Rev. Lett., 120, 172703
Arnett W. D., 1982, ApJ, 253, 785
Ashton G. et al., 2019, ApJS, 241, 27
Barbieri C., Salafia O. S., Perego A., Colpi M., Ghirlanda G., 2019, A&A, 625, A152
Barbieri C., Salafia O. S., Perego A., Colpi M., Ghirlanda G., 2020, Eur. Phys. J., A56, 8
Barnes J., Kasen D., Wu M.-R., Martínez-Pinedo G., 2016, ApJ, 829, 110
Barnes J., Zhu Y., Lund K., Sprouse T., Vassh N., McLaughlin G., Mumpower M., Surman R., 2020, preprint (arXiv:2010.11182)
Bauswein A., Goriely S., Janka H.-T., 2013, ApJ, 773, 78
Bauswein A., Stergioulas N., Janka H.-T., 2014, Phys. Rev. D, 90, 023002
Bauswein A., Just O., Janka H.-T., Stergioulas N., 2017, ApJ, 850, L34
Bernuzzi S., Nagar A., Balmelli S., Dietrich T., Ujevic M., 2014, Phys. Rev. Lett., 112, 201101
Bernuzzi S., Nagar A., Dietrich T., Damour T., 2015a, Phys. Rev. Lett., 114, 161103
Bernuzzi S., Dietrich T., Nagar A., 2015b, Phys. Rev. Lett., 115, 091101
Bernuzzi S. et al., 2020, MNRAS, 497, 1488
Bovard L., Martin D., Guercilena F., Arcones A., Rezzolla L., Korobkin O., 2017, Phys. Rev. D, 96, 124005
Breschi M., Bernuzzi S., Zappa F., Agathos M., Perego A., Radice D., Nagar A., 2019, Phys. Rev. D, 100, 104029
Capano C. D. et al., 2020, Nat. Astron., 4, 625
Cardelli J. A., Clayton G. C., Mathis J. S., 1989, ApJ, 345, 245
Chornock R. et al., 2017, ApJ, 848, L19
Coughlin M., Dietrich T., Kawaguchi K., Smartt S., Stubbs C., Ujevic M., 2017, ApJ, 849, 12
Coughlin M. W. et al., 2018, MNRAS, 480, 3871
Coughlin M. W., Dietrich T., Margalit B., Metzger B. D., 2019, MNRAS, 489, L91
Coulter D. A. et al., 2017, Science, 358, 1556
Cowperthwaite P. S. et al., 2017, ApJ, 848, L17
Damour T., Nagar A., Villain L., 2012, Phys. Rev. D, 85, 123007
de Jesús Mendoza-Temis J., Wu M.-R., Martínez-Pinedo G., Langanke K., Bauswein A., Janka H.-T., 2015, Phys. Rev., C92, 055805
De S., Finstad D., Lattimer J. M., Brown D. A., Berger E., Biwer C. M., 2018, Phys. Rev. Lett., 121, 091102
Decoene V., Guépin C., Fang K., Kotera K., Metzger B., 2020, J. Cosmol. Astropart. Phys., 04, 045

Del Pozzo W., Veitch J., 2021, johnveitch/cpnest: v0.11.3, Available at: https://github.com/johnveitch/cpnest
Dietrich T., Bernuzzi S., Brügmann B., Tichy W., 2018, in Part of Proceedings, 26th Euromicro International Conference on Parallel, Distributed and Network-based Processing (PDP 2018). p. 682, Available at: https://inspirehep.net/record/1663472/files/1803.07965.pdf
Dietrich T., Coughlin M. W., Pang P. T. H., Bulla M., Heinzel J., Issa L., Tews I., Antier S., 2020, Science, 370, 1450
Endrizzi A. et al., 2020, Eur. Phys. J. A, 56, 15
Essick R., Tews I., Landry P., Reddy S., Holz D. E., 2020, Phys. Rev. C, 102, 055803
Even W. et al., 2020, ApJ, 899, 24
Fernández R., Metzger B. D., 2013, MNRAS, 435, 502
Fernández R., Quataert E., Schwab J., Kasen D., Rosswog S., 2015, MNRAS, 449, 390
Fujibayashi S., Kiuchi K., Nishimura N., Sekiguchi Y., Shibata M., 2018, ApJ, 860, 64
Fujibayashi S., Wanajo S., Kiuchi K., Kyutoku K., Sekiguchi Y., Shibata M., 2020, ApJ, 901, 122
Gamba R., Bernuzzi S., Nagar A., 2020a, preprint (arXiv:2012.00027)
Gamba R., Breschi M., Bernuzzi S., Agathos M., Nagar A., 2020b, preprint (arXiv:2009.08467)
Ghirlanda G. et al., 2019, Science, 363, 968
Goodman J., Weare J., 2010, Commun. Appl. Math. Comput. Sci., 5, 65
Grossman D., Korobkin O., Rosswog S., Piran T., 2014, MNRAS, 439, 757
Hajela A. et al., 2019, ApJ, 886, L17
Hotokezaka K., Kiuchi K., Kyutoku K., Okawa H., Sekiguchi Y.-i., Shibata M., Tanuguchi K., 2013, Phys. Rev. D, 87, 024001
Hotokezaka K., Beniamini P., Piran T., 2018, Int. J. Mod. Phys., D27, 1842005
Jiang J.-L., Tang S.-P., Wang Y.-Z., Fan Y.-Z., Wei D.-M., 2020, ApJ, 892, 1
Just O., Obergaulinger M., Janka H. T., 2015, MNRAS, 453, 3386
Kasen D., Barnes J., 2019, ApJ, 876, 128
Kasen D., Badnell N. R., Barnes J., 2013, ApJ, 774, 25
Kasen D., Fernández R., Metzger B., 2015, MNRAS, 450, 1777
Kasen D., Metzger B., Barnes J., Quataert E., Ramirez-Ruiz E., 2017, Nature, 551, 80
Kawaguchi K., Shibata M., Tanaka M., 2020, ApJ, 889, 171
Korobkin O., Rosswog S., Arcones A., Winteler C., 2012, MNRAS, 426, 1940
Lippuner J., Roberts L. F., 2015, ApJ, 815, 82
Margalit B., Metzger B. D., 2017, ApJ, 850, L19
Martin D., Perego A., Arcones A., Thielemann F.-K., Korobkin O., Rosswog S., 2015, ApJ, 813, 2
Metzger B. D., 2020, Living Rev. Relativ., 23, 1
Metzger B., Berger E., 2012, ApJ, 746, 48
Metzger B. D., Fernández R., 2014, MNRAS, 441, 3444
Metzger B., Piro A., Quataert E., 2008, MNRAS, 390, 781
Metzger B. D., Arcones A., Quataert E., Martínez-Pinedo G., 2010, MNRAS, 402, 2771
Miller J. M. et al., 2019, Phys. Rev. D, 100, 023008
Nagar A. et al., 2018, Phys. Rev. D, 98, 104052
Nakar E., Gottlieb O., Piran T., Kasliwal M. M., Hallinan G., 2018, ApJ, 867, 18
Nedora V., Bernuzzi S., Radice D., Perego A., Endrizzi A., Ortiz N., 2019, ApJ, 886, L30
Nedora V. et al., 2020, preprint (arXiv:2011.11110)
Nedora V. et al., 2021, ApJ, 906, 98
Nelson B., Ford E. B., Payne M. J., 2013, ApJS, 210, 11
Nicholl M. et al., 2017, ApJ, 848, L18
Nynka M., Ruan J. J., Haggard D., Evans P. A., 2018, ApJ, 862, L19
Oechslin R., Janka H.-T., Marek A., 2007, A&A, 467, 395
Perego A., Rosswog S., Cabezon R., Korobkin O., Käppeli R., Arcones A., Liebendörfer M., 2014, MNRAS, 443, 3134
Perego A., Radice D., Bernuzzi S., 2017a, ApJ, 850, L37
Perego A., Yasin H., Arcones A., 2017b, J. Phys., G44, 084007
Perego A., Bernuzzi S., Radice D., 2019, Eur. Phys. J., A55, 124
Pian E. et al., 2017, Nature, 551, 67
Piran T., Nakar E., Rosswog S., 2013, MNRAS, 430, 2121
Raaijmakers G. et al., 2020, ApJ, 893, L21
Radice D., Dai L., 2019, Eur. Phys. J., A55, 50
Radice D., Galeazzi F., Lippuner J., Roberts L. F., Ott C. D., Rezzolla L., 2016, MNRAS, 460, 3255
Radice D., Bernuzzi S., Del Pozzo W., Roberts L. F., Ott C. D., 2017, ApJ, 842, L10
Radice D., Perego A., Bernuzzi S., Zhang B., 2018a, MNRAS, 481, 3670
Radice D., Perego A., Zappa F., Bernuzzi S., 2018b, ApJ, 852, L29
Radice D., Perego A., Hotokezaka K., Bernuzzi S., Fromm S. A., Roberts L. F., 2018c, ApJ, 869, L35
Radice D., Perego A., Hotokezaka K., Fromm S. A., Bernuzzi S., Roberts L. F., 2018d, ApJ, 869, 130
Roberts L. F., Kasen D., Lee W. H., Ramirez-Ruiz E., 2011, ApJ, 736, L21
Rosswog S., Piran T., Nakar E., 2013, MNRAS, 430, 2585
Rosswog S., Korobkin O., Arcones A., Thielemann F. K., Piran T., 2014, MNRAS, 439, 744
Rosswog S., Sollerman J., Feindt U., Goobar A., Korobkin O., Wollaeger R., Fremling C., Kasliwal M. M., 2018, A&A, 615, A132
Savchenko V. et al., 2017, ApJ, 848, L15
Shibata M., Taniguchi K., Uryu K., 2005, Phys. Rev. D, 71, 084021
Siegel D. M., Metzger B. D., 2018, ApJ, 858, 52
Sivia D. S., Skilling J., 2006, Data Analysis – A Bayesian Tutorial, 2nd edn. Oxford Science Publications, Oxford Univ. Press, Oxford
Skilling J., 2006, Bayesian Anal., 1, 833
Smartt S. J. et al., 2017, Nature, 551, 75
Smith R. J. E., Ashton G., Vajpeyi A., Talbot C., 2020, MNRAS, 498, 4492
Tanaka M. et al., 2017, PASJ, 69, 102
Tanaka M., Kato D., Gaigalas G., Kawaguchi K., 2020, MNRAS, 496, 1369
Tanvir N. R. et al., 2017, ApJ, 848, L27
Valenti S. et al., 2017, ApJ, 848, L24
Veitch J. et al., 2015, Phys. Rev. D, 91, 042003
Villar V. A., Berger E., Metzger B. D., Guillochon J., 2017a, ApJ, 849, 70
Villar V. A. et al., 2017b, ApJ, 851, L21
Winkler C., Diehl R., Ubertini P., Wilms J., 2011, Space Sci. Rev., 161, 149
Wollaeger R. T. et al., 2018, MNRAS, 478, 3298
Wu M.-R., Fernández R., Martínez-Pinedo G., Metzger B. D., 2016, MNRAS, 463, 2323
Zappa F., Bernuzzi S., Pannarale F., Mapelli M., Giacobbo N., 2019, Phys. Rev. Lett., 123, 041102
Zhu Y., Lund K., Barnes J., Sprouse T., Vassh N., McLaughlin G., Mumpower M., Surman R., 2021, AJ, 906, 94

This paper has been typeset from a TEX/LATEX file prepared by the author.